american physiological society
AMERICAN JOURNAL OF PHYSIOLOGY
CELL PHYSIOLOGY

Am J Physiol Cell Physiol 329: C1521–C1538, 2025.
First published September 27, 2025; doi:10.1152/ajpcell.00272.2025

RESEARCH ARTICLE

Exploring the molecular cargos associated with extracellular vesicles extracted from bone tissue to identify novel players in osteoblast function

Floriane Binet,[1]* Laura Entz,[1]* Meggane Amiot,[1] Solène Tessier,[1] Joëlle Véziers,[2] Laurence De Beaurepaire,[3,4] Gwennan André-Grégoire,[5,6] Florent Dingli,[7] Damarys Loew,[7] Pierre Weiss,[8] Angélique Galvani,[1]* and Valérie Geoffroy[1]*

[1]*Nantes Université, Oniris, Univ Angers, Inserm, RMeS, UMR 1229, Nantes, France;* [2]*Nantes Université, Oniris, CHU Nantes, Inserm, RMeS, UMR 1229, Nantes, France;* [3]*Oniris, INRAE, IECM, USC1383, Nantes, France;* [4]*Oniris, B-FHIT, Nantes, France;* [5]*Nantes Université, Inserm, CNRS, Univ Angers, CRCI2NA, Team SOAP, Nantes, France;* [6]*Institut de Cancérologie de l'Ouest, Saint-Herblain, France;* [7]*CurieCoreTech Mass Spectrometry Proteomics, PSL Research University, Institut Curie, Paris, France; and* [8]*Nantes Université, Oniris, Univ Angers, CHU Nantes, Inserm, RMeS UMR 1229, Nantes, France*

Abstract

Extracellular vesicles (EVs), composed of proteins, lipids, and nucleic acids, are key mediators of intercellular communication across various tissues. However, research on EVs isolated directly from bone tissue remains limited. Here, we identified for the first time and characterized two EV subpopulations extracted from bone tissue and enhanced our understanding of their roles in bone physiology. These two EV subpopulations were reproducibly isolated: a large EV population (lEV; 237.7 ± 8.8 nm) and a small EV population (sEV; 109.2 ± 8.3 nm), both exhibiting the expected shape and presence of EV and bone cell markers. Comparative analysis of their cargos revealed unique or enriched proteins and miRNA profiles for each, suggesting shared functional characteristics with bone cells, including osteocytes, osteoblasts, and osteoclasts. Notably, lEVs contained proteins such as FHL2 and pleiotrophin, along with miRNAs including miR-15b-5p, miR-29a-3p, and miR-128-3p, all of which are involved in early osteogenic signaling pathways such as Hippo, TGF-β, and Wnt. Furthermore, sEVs contained ALP, PAPSS2, and miR-125b, both known regulators of matrix mineralization. Both EV subpopulations were internalized by stromal ST2 and preosteoblastic MC3T3-E1 cells. We present evidence that lEVs significantly enhanced ALP activity in ST2 cells, indicating early osteogenic stimulation, whereas sEVs partially promoted matrix mineralization in primary osteoblasts. Our findings provide novel insights into the role of bone-derived EVs as possible complementary mediators of osteogenesis in vivo and highlight the potential of their cargos in advancing bone regeneration strategies.

NEW & NOTEWORTHY This study identifies for the first time two extracellular vesicle (EV) subpopulations isolated from young male mice bone tissue, with distinct mean size and molecular signature. Analysis of the protein and miRNA cargos of these EVs indicates that the large and small EVs are involved in different stages of osteogenesis, from commitment to the formation of mineralized tissue. These findings provide new insights into the role of bone-derived EVs in bone physiology.

bone; extracellular vesicles; osteogenesis; proteomics; small RNA sequencing

INTRODUCTION

Osteogenesis is a critical process for maintaining bone mass, quality, and regeneration. Central to this process are osteoblasts (bone-forming cells) and their mesenchymal progenitor cells, which drive the formation of new bone (1). Osteocytes, derived from mature osteoblasts, are highly specialized and multifunctional cells that constitute over 95% of all bone cells (2). Acting as key regulators and coordinators of osteogenesis, they play an essential role in maintaining the bone matrix and ensuring mineralization (3). These cells are embedded within a mineralized matrix and interconnected, forming a complex osteocytic network (4). Osteocytes function as mechanosensors, responding to extracellular signals such as fluid flow shear stress to trigger appropriate responses from effector cells, including osteoblasts, osteoclasts (bone-resorbing cells), and their precursors. Osteocytes thus serve as coordinators and primary regulators of bone remodeling, initiating remodeling cycles and facilitating crosstalk between osteoblasts and osteoclasts to maintain bone health.

The regulation of osteogenesis involves complex and dynamic interactions among various bone cells, forming a sophisticated regulatory network influenced by soluble factors that modulate osteoblastic activity. For example, Wnt antagonists such as sclerostin and dickkopf-related protein 1 (DKK-1) inhibit osteoblastogenesis, whereas signaling molecules such

*F. Binet and L. Entz contributed equally to this work. A. Galvani and V. Geoffroy contributed equally to this work.
Correspondence: A. Galvani (angelique.galvani@univ-nantes.fr).
Submitted 27 March 2025 / Revised 22 April 2025 / Accepted 18 September 2025

as nitric oxide (NO), ATP, and prostaglandin E2 (PGE2) promote anabolic responses in bone tissue (3, 5). Although the role of locally secreted soluble factors in osteogenesis is well-documented, recent research over the past decade has increasingly recognized extracellular vesicles (EVs) as critical regulators of bone formation and regeneration (6, 7).

EVs are heterogeneous particles released by cells, traditionally categorized by their biogenesis and size. The terms exosomes, which refer primarily to EVs of endosomal origin, and ectosomes or microvesicles, derived from plasma membrane budding, have historically been used. However, these classifications have been replaced by the designations of small EVs (sEVs, <200 nm) and large EVs (lEVs, >200 nm) (8).

EVs carry a diverse array of cargo, including soluble, membrane-bound, and transmembrane proteins, as well as coding and noncoding nucleic acids, lipids, and other cytosolic compounds such as ions and small organelles. The composition of these cargos is influenced by both the cellular origin of the EVs and their pathophysiological environment (9–11). EVs are crucial for intercellular communication, acting both locally and distally (12). Their potential role in communication among bone cells has been discussed in numerous publications (see Ref. 13 for review). EVs and their cargos are released by various bone cells and their precursors in vitro, including mesenchymal stem cells (MSCs) (14), osteoblasts (15, 16), osteocytes (17–19), and osteoclasts (20–22). These vesicles seem crucial to essential processes, ranging from bone remodeling (23, 24) to repair and regeneration (6, 25–27).

Among bone-derived vesicles, matrix vesicles (MVs) have been recognized since the 1970s as key mediators of bone extracellular matrix (ECM) mineralization. Despite their historical roles, there is no consensus on whether MVs should be classified as EVs (28). Some researchers argue that MVs and EVs overlap significantly in terms of biogenesis, composition, and function, making it challenging to distinguish between them (29). Conversely, recent studies have identified differences in size, protein composition, and function between MVs and EVs derived from osteoblastic cell lines in vitro, suggesting distinct roles and characteristics for these vesicle types (30).

The application of EVs in bone regeneration could represent a significant advancement, offering more effective and safer therapeutic options compared with traditional cell therapies. However, further research is necessary to better understand the mechanisms and cargos involved in EV function in vivo, as well as to mitigate potential adverse effects such as tumorigenesis and inflammation. Another promising approach is to exploit the bioactive molecules within EVs that are implicated in the physiological mechanisms of bone regeneration.

Most of the knowledge regarding the molecular cargos of EVs derived from bone cells stems from in vitro studies (31, 32), and our understanding of the delivery of molecular cargos by EVs to enhance or stimulate osteogenesis is still limited. Therefore, this study aims to investigate EVs isolated from mouse long bones in vivo and to provide initial information on their osteogenic potential in vitro by identifying their protein and microRNA (miRNA) cargos. Given their great diversity and small numbers, ascribing a specific biological effect to a given EV is particularly difficult because EVs evolve in number, space, and time within the tissue, following the dynamic evolution of the cells they contain. It is more likely that EVs derived from the different bone cells, present altogether in the extracellular fluid, have a common or even synergistic action on the recipient cells, which, in addition, may or may not be specifically targeted.

To this end, we established an approach to extract EVs directly from murine long bones, thereby minimizing biases associated with in vitro culture systems and allowing us to examine vesicles produced under physiological conditions. To investigate the properties of these heterogeneous vesicles, we used a differential ultracentrifugation approach to separate them into subpopulations based on size and density, called large and small EVs. We noted that available literature has focused mainly on small vesicles (exosomes and matrix vesicles) extracted from bone, leaving the potential role of larger EVs less well characterized. We compared these two subpopulations of EVs based on their protein and miRNA content. Proteomic analysis showed that lEVs and sEVs had similar core components, but also displayed distinct molecular profiles, including skeletal-related pathways. Although the two EV types shared most of their miRNA content, differential enrichment of selected miRNAs was identified. Observed in vitro, the effects of the two EV subpopulations on stromal cell differentiation and osteoblastic activity suggest a complementary role in osteogenesis and beyond. These results contribute to a better understanding of the complexity and diversity of bone-derived EVs and their potential involvement as a whole in the physiological regeneration mechanisms of bone tissue.

MATERIALS AND METHODS

Isolation of EVs from Bone

SWISS mice (Janvier Labs) were housed in the Nantes University Unité de Thérapeutique Expérimentale de l'Institut de Recherche en Santé de Nantes Université (UTE IRS-UN) animal facility under specific pathogen-free conditions, adhering to institutional guidelines (Accreditation Number C44-278). All procedures were conducted in compliance with French and European regulations regarding the care and protection of laboratory animals (EC Directive 86/609, French Law 2001-486 of June 6, 2001).

EVs were extracted from the tibias and femurs of 8-wk-old male SWISS mice following the protocol established by Balcerzak et al. (33). However, to preserve the integrity of protein content and reduce the risk of altering EV cargo, Balcerzak's protocol was adapted by removing enzymatic digestion and bone perfusion. After carefully removing all surrounding soft tissue and cutting the epiphyses, the bones were centrifuged at 14,000 *g* for 3 s to eliminate bone marrow. The bones were then crushed using a PT 10–35 GT, Polytron at 336 *g* for 10 s. The resulting supernatant was centrifuged at 700 *g* for 10 min to remove bone debris, followed by a second centrifugation at 2,000 *g* for 10 min to eliminate tissue debris. The supernatant, referred to as the total fraction (total), was ultracentrifuged at 100,000 *g* for 70 min to separate the total vesicular fraction (pellet) (EVtot) from the non-EV fraction (non-EV). The preparation of EV subpopulations was adapted from a differential ultracentrifugation protocol (34). The total fraction was first centrifuged at

10,000 *g* for 30 min. The resulting pellet was washed with phosphate-buffered saline (PBS) at 10,000 *g* for 30 min to isolate a subpopulation of lEVs. The supernatant was then ultracentrifuged on a 30% PBS-sucrose cushion at 100,000 *g* for 70 min. The interface between the supernatant and the PBS-sucrose cushion was collected and further washed in PBS at 100,000 *g* for 70 min to obtain a population of sEVs. All centrifugation steps were performed at 4°C. The separated EV fractions were resuspended in PBS, aliquoted, and stored at 4, −20, or −80°C before use for cell treatments, and miRNA and protein content analyses, respectively.

Scanning Transmission Electron Microscopy Analysis

EVs were examined using negative stain electron microscopy. EVs were first incubated for 20 min on Formvar/carbon-coated copper 200 mesh grids (AGS162, Agar Scientific). The grids were then washed with PBS and fixed with 1% glutaraldehyde (G5882, Sigma-Aldrich) in PBS for 5 min. After eight washes with PBS, the samples were stained with Uranyless (Delta Microscopies) for 1 min. The grids were subsequently coated with a thin layer of platinum (0.8 nm) using a Leica EM ACE600 high vacuum sputter coater. The negatively stained grids were analyzed using a GeminiSEM 300 Zeiss scanning electron microscope equipped with a scanning transmission electron microscopy (STEM) detector. Observations were conducted at 27 keV with a 7.5 μm diaphragm and a working distance of 4.5 mm.

Particle Measurements

The size and concentration of EVs were determined using tunable resistive pulse sensing (TRPS) technology (Izon Science). For this analysis, thermoplastic polyurethane nanopores NP400 and NP150 were used to measure the lEV and sEV populations, respectively. Samples were diluted in PBS containing 0.03% Tween-20, and measurements were taken at multiple pressures to ensure accuracy. Calibration of the TRPS system was conducted using CPC400 and CPC200 standards.

Protein Measurements and Western Blot Analysis

Total protein content in the EVs was quantified using a micro-BCA assay kit (Cat. No. 23235; Thermo Fisher Scientific) following the manufacturer's instructions.

For western blot analysis, 3 or 5 μg of protein from each EV sample was denatured in 6× Laemmli buffer (Bio-Rad). As a positive cell control, 10 or 15 μg of protein from primary osteoblasts (POBs) and primary bone cells were used and denatured in 6× Laemmli buffer (Bio-Rad). Proteins were then separated using precast 4%–15% polyacrylamide Mini-PROTEAN TGX Stain-free gels under nonreducing conditions (for tetraspanins CD9 and CD81) or reducing conditions (for all other proteins). Following separation, proteins were transferred to PVDF membranes (Bio-Rad) for further analysis.

Membranes were blocked in Tris-buffered saline with Tween (TBST) containing 5% nonfat dry milk for 1 h. They were then incubated overnight at 4°C with primary antibodies diluted in TBST with 5% nonfat dry milk. The primary antibodies used were as follows: anti-cadherin-2 (CADH2) (Cat. No. ab18203, RRID:AB_44431, 1:1,000; Abcam), anti-Calnexin (Cat. No. GTX109669, RRID:AB 1949824, 1:1,000; GeneTex), HRP anti-Cathepsin K (Cat. No. sc-48353, RRID: AB_2087687,1:1,500; Santa Cruz Biotechnology), anti-CD9 (Cat. No. ab82390, RRID:AB_2244514, 1:1,000; Abcam), anti-CD81 (Cat. No. 104901, RRID:AB_313136, 1:1,000; BioLegend), HRP anti-Flotillin-1 (FLOT-1) (Cat. No. 849803, RRID:AB_2728577, 1:2,500; BioLegend), anti-130 kDa cis-Golgi matrix protein 1 (GM130) (Cat. No. 610823, RRID:AB_398142, 1:500; BD Biosciences), anti-lysosomal-associated membrane protein 1 (LAMP-1) (Cat. No. ab24170, RRID:AB_775978, 1:1,000; Abcam), anti-p84 (Cat. No. ab487, RRID:AB_304696, 1:1,000; Abcam), anti-Podoplanin (Cat. No. ab131216, RRID:AB_11157489, 1:1,000; Abcam), and anti-receptor activator of nuclear factor kappa-B ligand (RANKL) (Cat. No. sc-377079, RRID:AB_3678560, 1:1,000; Santa Cruz Biotechnology). After primary antibody incubation, the membranes were washed three times with TBST and then incubated for 1 h with secondary antibodies diluted in TBST with 5% nonfat dry milk. The secondary antibodies included anti-goat (Cat. No. HAF019, RRID:AB_573132, 1:10,000; R and D Systems), anti-hamster (Cat. No. PA1-32045, RRID:AB_10985178, 1:20,000; Thermo Fisher Scientific), anti-mouse (Cat. No. A9917, RRID: AB_258476, 1:100,000; Sigma-Aldrich), anti-rabbit (Cat. No. 7074, RRID:AB_2099233, 1:20,000 or 1:50,000; Cell Signaling Technology), and anti-rat (Cat. No. 712-035-153, RRID:AB_2340639, 1:100,000; Jackson ImmunoResearch Labs).

Detection was performed using SuperSignal West Femto Maximum Sensitivity Substrate (Cat. No. 34095; Thermo Fisher Scientific) and visualized with a ChemiDoc Imaging System (Bio-Rad).

Primary Cells Preparation and Cell Culture Conditions

The study used the murine bone marrow-derived stroma cell line ST2 (Research, Lot 5, RRID:CVCL_2205; German Collection of Microorganisms and Cell Cultures GmbH), the murine preosteoblastic cell line MC3T3-E1 (ATCC, CRL-2593, subclone 4, RRID:CVCL_0409), and POBs.

POBs were isolated from the *calvariae* of 2- to 4-day-old SWISS mice as previously described (35). Briefly, *calvariae* were first digested with 0.2% type IV collagenase (Sigma-Aldrich) in PBS supplemented with ethylenediaminetetraacetic acid (EDTA) for 15 min to remove fibroblasts. They were then further digested with 0.2% type IV collagenase in PBS for 1 h to specifically release osteoblastic cells. These osteoblastic cells were expanded for 5–6 days in α-modified Eagle's medium (α-MEM, Biowest) supplemented with 10% fetal bovine serum (FBS) (PAN-Biotech), 1% penicillin/streptomycin (Thermo Fisher Scientific), and 1% L-glutamine (Biowest). For experiments involving EVs, the FBS used was depleted of EVs through ultracentrifugation at 100,000 *g* overnight.

Primary bone cells were isolated from the tibias and femurs of 8-wk-old male SWISS mice. The bones were digested with 0.2% type IV collagenase (Sigma-Aldrich) in PBS supplemented with 4 mM EDTA for 10 min at 37°C, then rinsed with PBS. This step was repeated four times. The samples were first centrifuged at 259 *g* for 5 min and then at 10,000 *g* for 1 min. The cell pellet was resuspended in lysis buffer to serve as a control for western blot analysis.

The ST2 and MC3T3-E1 cell lines were seeded at a density of 1×10^4 cells/cm^2 for the uptake experiments. After 48 h, 5,000 ng of lEVs proteins, corresponding to 3.76×10^8 EVs,

and 5,000 ng of sEVs proteins, corresponding to 3×10^9 EVs, were added to the medium.

For alkaline phosphatase (ALP) assays, the ST2 cell line, not yet committed to the osteoblastic lineage, and the MC3T3-E1 cell line, already committed to the osteoblastic lineage, was seeded at a density of 1.6×10^4 cells/cm^2 and 3×10^4 cells/cm^2, respectively. After 24 h, osteogenic differentiation was induced by adding 50 μM ascorbic acid and 10 mM β-glycerophosphate (Sigma-Aldrich), designated as *day 0*. For experiments involving the total, EVtot, and non-EV fractions, 7,500 ng of proteins were added to the medium at *day 0*. For ALP assays with both lEVs and sEVs, three different concentrations were tested: 1× (4.2×10^7 EVs/cm^2), 10× (4.2×10^8 EVs/cm^2), and 50× (2.1×10^9 EVs/cm^2).

For RNA extraction, ST2 or MC3T3-E1 cells were seeded at a density of 2.4×10^4 cells/cm^2. The osteogenic differentiation protocol and the concentrations of lEVs and sEVs tested were consistent with those used for the ALP assays.

Finally, POBs were plated at a density of 2.6×10^4 cells/cm^2 for mineralized nodule formation assays. After 24 h, osteogenic differentiation was initiated by adding 50 μM ascorbic acid and 10 mM β-glycerophosphate (Sigma-Aldrich). Simultaneously, 3.5×10^8 EVs/cm^2 were introduced into the medium. The medium was replaced every 3–4 days, with fresh EVs added.

EV Labeling and Uptake Assays

EVs were labeled using MemGlow 640 (Cat. No. MG04-02; Cytoskeleton, Inc.) following the manufacturer's protocol. In brief, the labeling solution was diluted 1:100 in the EV suspension and incubated in the dark on a rotating wheel for 30 min. Post labeling, the suspension was centrifuged to separate the EVs at 10,000 *g* for 30 min for lEVs and 100,000 *g* for 70 min for sEVs. The same procedure was performed using PBS instead of EV suspension to generate the experimental control (CTL). The resuspension solution, with or without the labeled EVs, was then added to the cell culture medium and incubated with the cells for 4 h in the dark. After incubation, cells were fixed with 4% paraformaldehyde (PFA) for 5 min at room temperature (RT), and the nuclei were stained with Hoechst diluted 1:5,000 (Invitrogen) for 15 min at RT. The cells were then mounted in ProLong Gold antifade reagent (Invitrogen) and examined using a Nikon A1 confocal microscope equipped with a ×60/1.4 oil immersion objective. Imaging was controlled using Nikon Imaging Software (NIS) Elements software. Large images covering nine adjacent fields of view were captured and processed using the NIS built-in registration algorithm to properly stitch the images. High-resolution images were recorded with the ×60/1.4 oil objective, in accordance with the Nyquist sampling rate at 70 nm/pixel. These images were then deconvolved using the Lucy Richardson algorithm provided by the NIS software.

Cell morphology and structure features were observed using the laser scanning confocal microscope's reflection modality, maintaining the same resolution as that used for fluorescence imaging. The interface between biological structures and the coverslip produces a strong reflective contrast signal. Descanning of the reflected excitation light (405 nm laser beam) to a detector enabled precise visualization of unstained structures.

Total RNA Isolation of ST2 and MC3T3 Cell Lines and RT-qPCR

Total RNA was extracted using the NucleoSpin RNA XS kit (Cat. No. 740990; Macherey-Nagel) according to the manufacturer's instructions. RNA yield was quantified with a NanoDrop 1000 spectrophotometer (Thermo Fisher Scientific). For each sample, 500 ng of total RNA was reverse-transcribed using the Verso cDNA Kit (Cat. No. AB1453; Thermo Fisher Scientific) with a combination of random primers and oligo dT. Real-time quantitative PCR (RT-qPCR) was conducted using the ABsolute Blue QPCR SYBR Green master mix (Cat. No. AB4166B; Thermo Fisher Scientific) in triplicate. Primer sequences are listed in Supplemental Table S1. qPCR was performed with a CFX96 Touch Deep Well 374 Real-Time PCR Detection System (Bio-Rad). The relative expression levels of Osterix (*Osx*) and Osteocalcin (*Ocn*) mRNA were normalized to the housekeeping genes TATA-box binding protein (*Tbp*) and tyrosine 3-monooxygenase/tryptophan 5-monooxygenase activation protein zeta (*Ywhaz*). Expression levels were calculated as fold changes relative to −EVs at *day 0* control condition.

Alkaline Phosphatase Activity Measurement

ALP activity was assessed in ST2 cell lysates following a freeze-thaw cycle and in EV subpopulations extracted from bone. The ALP activity was quantified using an ALP substrate kit (Cat. No. 1721063; Bio-Rad), with results expressed as nmol of *p*-nitrophenyl phosphate (PNP) hydrolyzed per minute. To normalize the data, total protein content was determined using a BCA protein assay kit (Cat. No. 23225; Thermo Fisher Scientific) for cell lysates and a micro-BCA protein assay kit (Cat. No. 23235; Thermo Fisher Scientific) for EVs, following the manufacturer's protocols. ALP activity was expressed as nmol PNP per mg of protein per minute (nmol PNP/mg protein/min). Alternatively, ALP activity measured in EVs was normalized to the number of EVs and was expressed as nmol PNP/10^6 EVs/min.

Mineralization Assay

Mineralized nodule formation in POBs was evaluated after 3 wk of culture in osteogenic medium. Following fixation with 4% PFA for 15 min at 4°C, the mineralized extracellular matrix was stained with Alizarin Red S (Sigma-Aldrich). To quantify the mineralized nodules, the stained samples were incubated in 10% acetic acid for 15 min with agitation to elute the calcium-bound dye. The optical density of the elute was measured at 450 nm.

Proteomics and Mass Spectrometry Analysis

Sample preparation.

Each sample was initially dried and resuspended in 10 μL of 8 M urea and 200 mM ammonium bicarbonate. The samples were then reduced with 5 mM dithiothreitol at pH 8.0 and 37°C for 1 h with vortexing. After cooling to RT, 10 mM iodoacetamide was added for alkylation in the dark for 30 min. Subsequently, the samples were diluted with 100 mM ammonium bicarbonate, pH 8.0, to reach a final urea concentration of 1 M. The samples were then digested overnight at 37°C using 0.2 μg of trypsin/LysC (Promega) with continuous vortexing. The digested samples were loaded onto homemade C18 Tips, which were packed by stacking three AttractSPE Disks (No.

SPE-Disk-Bio-C18; Affinisep) for desalting. Peptides were eluted using 40/60 MeCN/H_2O with 0.1% formic acid, followed by vacuum concentration to dryness. The samples were then reconstituted in 10 μL of injection buffer (0.3% trifluoroacetic acid), and 2 μg of each sample were analyzed by liquid chromatography-tandem mass spectrometry (LC-MS/MS).

LC-MS/MS analysis.

Online chromatography was performed using an RSLCnano system (Ultimate 3000; Thermo Scientific) coupled to an Orbitrap Eclipse mass spectrometer (Thermo Scientific). Peptides were initially trapped on a C18 column (75 μm inner diameter × 2 cm; nanoViper Acclaim PepMap 100; Thermo Scientific) with buffer A (2/98 MeCN/H_2O in 0.1% formic acid) at a flow rate of 3 μL/min for 4 min. Separation was then performed on a 50 cm × 75 μm C18 column (nanoViper Acclaim PepMap RSLC, 2 μm, 100 Å; Thermo Scientific) regulated to a temperature of 50°C using a linear gradient from 2% to 25% buffer B (100% MeCN in 0.1% formic acid) over 91 min at a flow rate of 300 nL/min. MS1 data were collected in the Orbitrap [120,000 at m/z 200 resolution; maximum injection time (IT) 60 ms; auto gain control (AGC) 4×10^5]. Charge states between 2 and 7 were required for MS2 analysis, and a 60-s dynamic exclusion window was applied. MS2 scans were performed in the ion trap in rapid mode with HCD fragmentation (isolation window 1.2 Da; normalized collision energy (NCE) 30%; IT 60 ms; AGC 10^4).

Mass spectrometry data analysis.

For identification, the data were searched against the *Mus musculus* (UP000000589_10090) UniProt (RRID:SCR_002380) database and a common contaminants database containing 245 proteins using Sequest-HT through Proteome Discoverer (version 2.4, RRID:SCR_014477). The enzyme specificity was set to trypsin, with a maximum of two missed cleavages allowed. Oxidized methionine, Met-loss, Met-loss-acetyl, and N-terminal acetylation were set as variable modifications, whereas carbamidomethylation of cysteines was set as a fixed modification. The maximum allowed mass deviation was set to 10 ppm for monoisotopic precursor ions and 0.6 Da for MS/MS peaks. The resulting files were further processed using myProMS v. 3.10.0 (36) (https://github.com/bioinfo-pf-curie/myproms). The false discovery rate (FDR) was calculated with Percolator (RRID:SCR_005040) (37) and set to 1% at the peptide level for the entire study. Label-free quantification was performed by peptide-extracted ion chromatograms (XICs), re-extracted under conditions and computed with MassChroQ version 2.2.21 (RRID:SCR_026669) (38). For protein quantification, XICs from proteotypic peptides shared between compared conditions (TopN matching) and missed cleavages were allowed. Median and scale normalization were applied to the total signal to correct the XICs for each biological replicate, accounting for total signal and global variance biases. To estimate the significance of changes in protein abundance, a linear model adjusted on peptides and biological replicates was generated, and P values were adjusted using the Benjamini–Hochberg FDR procedure.

Proteins were selected for sample comparison if they presented at least three distinct peptides in three biological replicates of both states. Proteins with an adjusted P value ≤ 0.05 were considered significantly different in the sample comparisons. Specific proteins unique to a condition were also considered if they met the peptide criteria. For other bioinformatic analyses, label-free quantification (LFQ) was performed using the previously described algorithm (39) for each sample after peptide XIC normalization as detailed earlier. The resulting LFQ intensities were used as indicators of protein (all peptides ≥ 2) abundance. For Principal Component Analysis (PCA) analyses, datasets were further filtered to remove entities with more than 34% of the values missing across all the samples used. The LFQ values were log10-transformed, and remaining missing values were imputed using the missMDA R package (40) to create complete matrices. Protein clustering (rows) was based on scaled log10-transformed LFQ value correlations, and Euclidean distances were calculated for clustering samples (columns).

Proteins are further analyzed and subjected to gene ontology (GO) functional enrichment analysis using MyProMS v. 3.10.0 (RRID:SCR_026670). Protein-protein interaction networks were generated using the STRING (Search Tool for the Retrieval of Interacting Genes/Proteins) database v. 12.0 (RRID:SCR_005223; https://string-db.org/) (41).

In addition, Kyoto Encyclopedia of Genes and Genomes (KEGG) pathway analysis was performed using DAVID v. 6.8 (RRID:SCR_001881; https://david.ncifcrf.gov/home.jsp) (42, 43) with proteins identified by at least three distinct peptides in at least one biological replicate of each state.

Small RNA-Seq Analysis of EVs and MicroRNA Target Gene Analysis

Total RNA from three replicates of lEVs and sEVs was extracted using a miRNeasy Mini Kit (Cat. No. 217084; Qiagen) following the manufacturer's instructions. The quality and concentration of the extracted RNA were determined using a small RNA chip on an Agilent 2100 Bioanalyzer (Agilent Technologies), according to the manufacturer's instructions. For library construction, 1–5 ng of the small RNA fraction (<200 nucleotides) was processed using the Qiaseq miRNA library prep kit (Qiagen) in accordance with the manufacturer's instructions. In brief, 3′ and 5′ adapters were ligated to each end of the RNA molecules, which were then reverse-transcribed and amplified to generate a cDNA library. Each library was quality-controlled using a high-sensitivity HS DNA chip. The libraries were sequenced on an Illumina MiSeq instrument using 75-base-length reads in single-read mode. After sequencing, a primary analysis was conducted using AOZAN software (ENS, Paris) to demultiplex and assess the quality of the raw data, based on FastQC modules (version 0.11.5).

The Fastq files were processed using miRge3.0 with the miRBase v22 *Mus musculus* GRCm38 reference (accession NCBI_Assembly:GCA_000001635.2). Statistical analyses of the read counts were performed using R (version 3.6.3) and the DESeq2 package (DESeq2_1.26.0) to determine the proportion of differentially expressed miRNAs between the two conditions. The standard DESeq2 normalization method (DESeq2's median of ratios with the DESeq function) was used. Following the package recommendations, the Wald test was used with the contrast function, and the Benjamini–Hochberg FDR control procedure was applied to identify the differentially expressed miRNAs.

For analysis, miRNAs were selected for sample comparison if they had at least 10 counts in three replicates of both

states. KEGG pathway analysis was performed using DIANA-miRPath v. 4.0 (RRID:SCR_017354) (44) using predicted conserved targets identified with the TargetScan Mouse v. 8.0 database.

Statistical Analysis

The number of experiments (N) and experimental replicates (n) are specified in the figure legends. Initially, potential outliers were identified using the ROUT method and excluded from the datasets. Data normality was assessed using the Shapiro–Wilk test. For statistical analysis performed on data obtained from more than seven independent experiments, a two-way ANOVA was conducted. When significant overall differences were detected by ANOVA, post hoc Tukey's test was used to examine differences between experimental conditions. A paired t test was used specifically to compare ALP activity differences in EV subpopulations between independent experiments. The nonparametric Kruskal–Wallis test with Dunn's post hoc test was applied for the data obtained from fewer than seven independent experiments or for the data that did not meet the normality assumption. Statistical significance was determined as a P value ≤ 0.05. All individual data points are presented, and the mean or median is shown when statistical analysis was performed using a parametric or nonparametric test, respectively. For ALP assay and gene expression determination, two-way ANOVA was used to assess overall variation and P values that could be attributed to EV subpopulations and treatment time. Statistical analyses were performed using Prism version 10.2.1 (RRID:SCR_002798; GraphPad Software).

RESULTS

Isolation and Characterization of Two Subpopulations of EVs from Bone Tissue

To explore the potential osteogenic properties of bone-derived EVs, we isolated EVs from young male mouse femurs and tibias (Fig. 1*A*). Interestingly, less than 10% of the proteins extracted from long bones were associated with the fraction containing the EVs (EVtot; Fig. 1*B*). However, when we evaluated osteoblastic differentiation by the three fractions by measuring ALP activity, an early marker of osteogenesis, in ST2 cells, the EVtot fraction was the only one to significantly increase ALP activity 1 and 3 days after induction (Fig. 1*C*). To elucidate the source of this effect, we compared the biological activity of subpopulations isolated from the EVtot fraction based on size and density, using targeted approaches.

These two subpopulations of EVs, called small and large EVs, were isolated using a modified differential ultracentrifugation protocol (33). A 30% sucrose cushion was added during the 100,000 *g* fraction isolation step to minimize coisolation of protein aggregates (Fig. 2*A*). Both subpopulations were characterized according to the Minimal Information for Studies of Extracellular Vesicles (MISEV) criteria (8). Single-particle analysis by the TRPS method showed an asymmetric particle size distribution (Fig. 2*B*), with distinct mode diameters for the two subpopulations named lEVs (237.7 ± 8.8 nm) and sEVs (109.2 ± 8.3 nm) (Fig. 2*C*). STEM revealed that both lEVs and sEVs exhibited spherical and cup-shaped morphologies typical of EVs (Fig. 2*D*) and with a recovery of $8.2 \pm 3.5 \times 10^8$ and $16.1 \pm 5.9 \times 10^8$ EVs per hindlimb for lEVs and sEVs, respectively (Fig. 2*E*). In addition, the amount of protein per million EVs was significantly higher in the lEV subpopulation compared with the sEV subpopulation (13.3 ± 9.6 ng/million EVs vs. 1.7 ± 0.5 ng/million EVs; Fig. 2*F*).

Molecular Composition of lEV and sEV

We investigated the protein profiles of both populations using mass spectrometry on EVs from three independent productions. Principal component analysis (PCA) revealed that the three lEV and sEV replicates clustered separately, indicating distinct and good reproducibility in protein compositions and thus in EV isolation (Fig. 3*A*). Proteomic analysis identified a total of 998 proteins in lEVs (Supplemental Table S2)

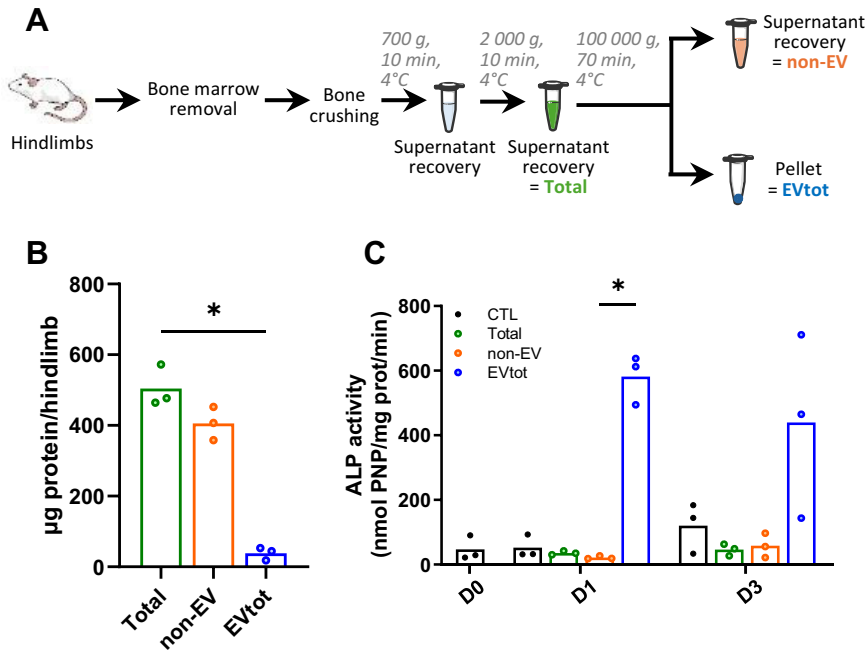

Figure 1. Extraction and evaluation of total bone-derived EV fraction (EVtot) and its osteogenic potential. *A*: schematic representation of the extraction process for EVtot from pools of 20 hindlimb long bones of 8-wk-old male SWISS mice. *B*: average protein content in the total, non-EV, and EVtot fractions, reported per hindlimb ($N = 3$, $n = 2$). *C*: ALP activity of ST2 stromal cells cultured under osteogenic conditions, measured at 1 day (D1) and 3 days (D3) post-treatment with PBS (CTL) or 7,500 ng prot/well of the total, non-EV, and EVtot fractions ($N = 3$, $n = 4$ or 5). Results are presented as a scatter plot with bars at the median and individual values indicated. Statistical significance was assessed using the nonparametric Kruskal–Wallis test followed by Dunn's post hoc test (*$P < 0.05$). ALP, alkaline phosphatase; CTL, control; EV, extracellular vesicle; PBS, phosphate-buffered saline.

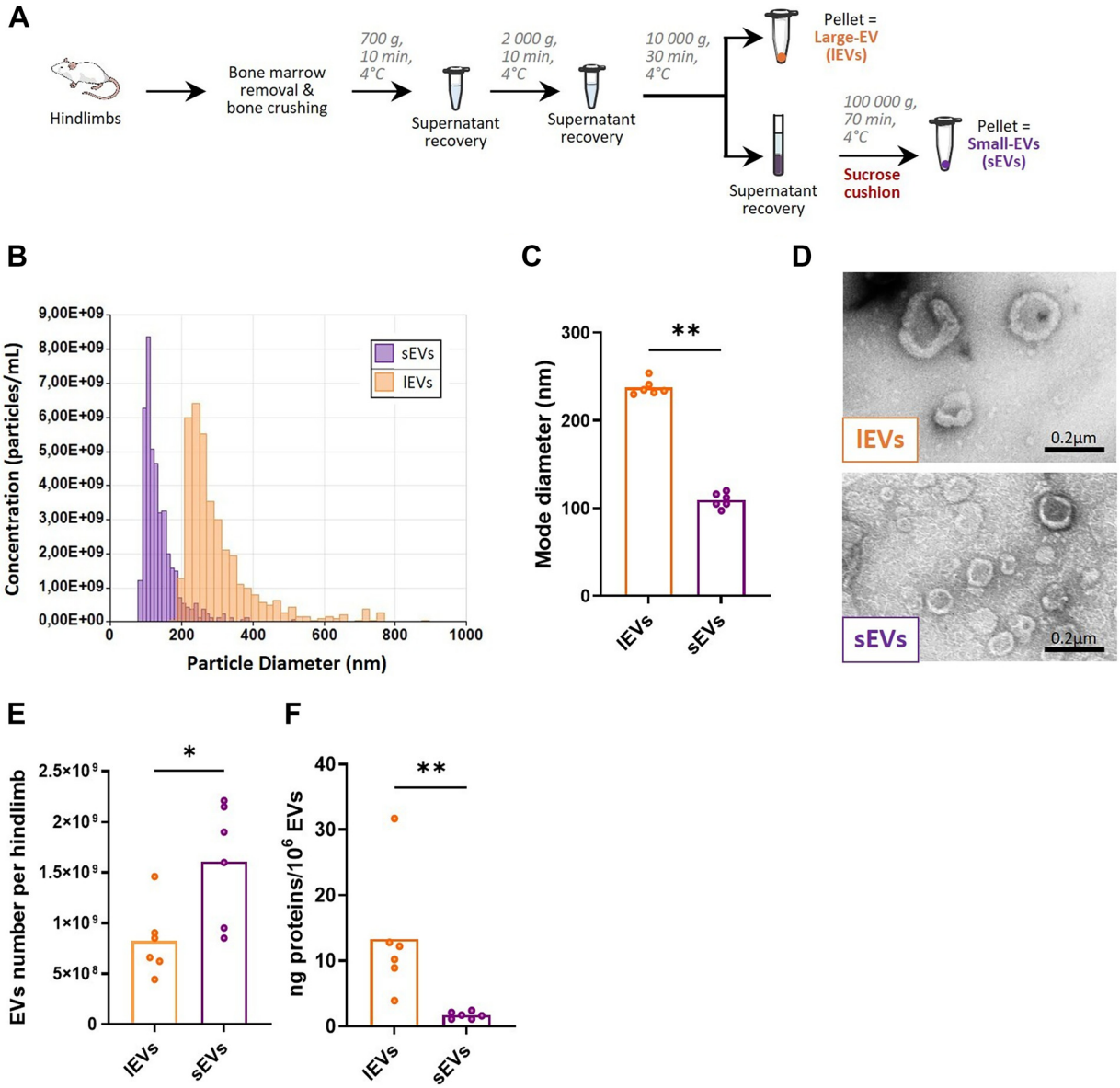

Figure 2. Physical and biochemical characterization of lEV and sEV subpopulations isolated from bone tissue. *A*: schematic representation of the isolation method for bone-derived EV subpopulations from pools of hindlimb long bones of 8-wk-old male SWISS mice. *B*: representative size distribution diagram of the particles, illustrating the range of particle sizes. *C*: mode particle diameter for the two EV subpopulations. *D*: scanning transmission electron microscopy images showing bone-derived lEVs and sEVs. *E*: quantity of lEVs and sEVs recovered per hindlimb. *F*: protein recovery per million particles of lEVs and sEVs. For *C*, *E*, and *F*, scatter plots with bars at the median and individual values from 5 to 6 independent EV preparations are shown. Comparisons were made using the nonparametric Mann–Whitney test for unpaired values (*$P < 0.05$; **$P < 0.005$). Panel *D* reproduced from Ref. 45. EV, extracellular vesicle; lEV, large EV population; sEV, small EV population.

and 1,069 proteins in sEVs (Supplemental Table S3), with 897 proteins shared between the two, 101 unique to lEVs and 172 unique to sEVs (Fig. 3*B*; Supplemental Fig. S1). Among the shared proteins, 596 exhibited significant differential abundance (adjusted P value < 0.05, including 108 proteins enriched in lEVs and 188 enriched in sEVs).

GO analysis of the shared and unique proteins (697 in lEVs and 768 in sEVs) revealed that proteins from both subpopulations are associated with GO terms related to vesicle and vesicular transport (Supplemental Fig. S2). In addition, 64% of the most abundant proteins identified in EVs across all studies published in the Vesiclepedia database (http://microvesicles.org/extracellular_vesicle_markers) were present in our EV subpopulations, including heat shock protein 90 (HSP90), annexin A1 (ANXA1), PDCD6IP (also known as Alix), and FLOT1. Moreover, we showed by western blot analysis the presence of EV-specific markers, including CD9, CD81, and LAMP-1. In addition, the intravesicular protein flotillin-1 was detected in both subpopulations (Fig. 3*C*). Interestingly, no signal was detected for markers of the nuclear (p84) or Golgi (GM130) compartments. However, calnexin, an endoplasmic reticulum marker, was present in both subpopulations (Fig. 3*D*). This proteomic profiling confirmed the vesicular nature of both subpopulations.

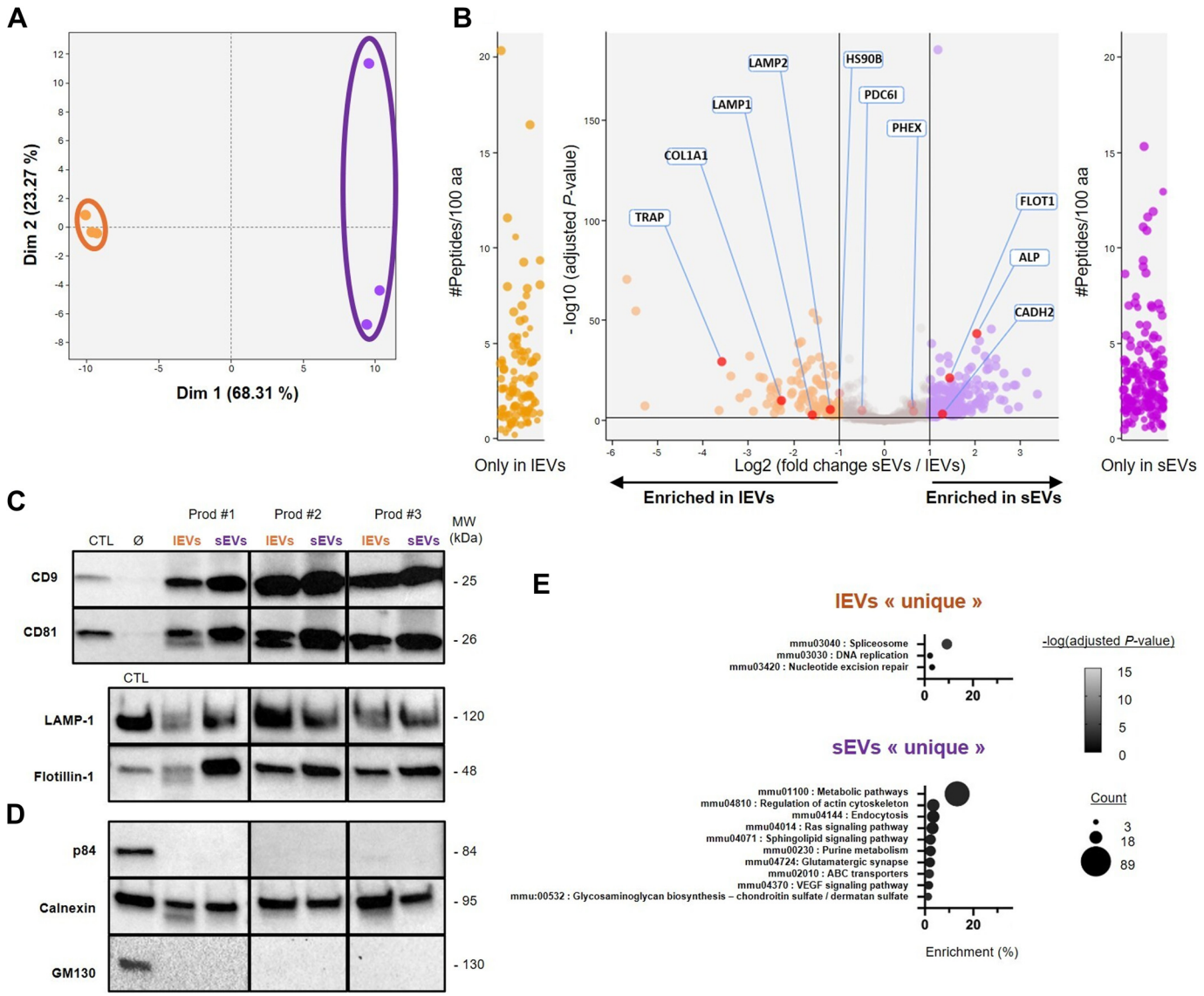

Figure 3. Quantitative proteomic analysis of lEV and sEV subpopulations isolated from bone tissue. *A*: principal component analysis of protein profiles from three replicates of lEV (orange) and sEV (purple) isolated from pools of 20 hindlimbs of 8-wk-old SWISS male mice. *B*: volcano plot illustrating the differential protein composition between lEVs and sEVs. The *y*-axis represents the adjusted *P* value (−log10), and the *x*-axis shows the fold change between the two EV subpopulations. Vertical lines denote log2 fold changes of −1 and 1. Proteins unique to each subpopulation are displayed on the *left* (lEVs) and *right* (sEVs) sides of the plot. Proteins specific to or enriched in lEVs and sEVs are highlighted in orange and purple, respectively. Examples of known bone cell-expressed proteins and EV markers are indicated. *C*: Western blot analysis of vesicular markers in lEV and sEV subpopulations. *D*: Western blot analysis of intracellular compartment markers in lEVs and sEVs, including p84 (nucleus), calnexin (endoplasmic reticulum), and GM130 (Golgi apparatus). All western blot analyses were performed on the same sets of EVs isolated from pools of 30–40 hindlimbs from 8-wk-old SWISS male mice in 3 independent experiments (prod no. 1, no. 2, and no. 3). Control (CTL) corresponds to proteins extracted from mouse calvaria primary osteoblasts. *E*: the associated KEGG pathways (based on adjusted *P* value) for the unique proteins for lEVs and sEVs are presented. The *y*-axis lists the terms, whereas the *x*-axis represents the enrichment level, indicating the percentage of proteins associated with each term in the analysis. The size of each circle reflects the number of proteins. Data were derived from three independent proteome replicates. EV, extracellular vesicle; KEGG, Kyoto Encyclopedia of Genes and Genomes; lEV, large EV population; sEV, small EV population.

Proteomic analysis revealed the presence of several bone-related proteins, including phosphate regulating endopeptidase X-linked (PHEX), collagen type I alpha 1 chain (COL1A1), ALP, CADH2, and tartrate-resistant acid phosphatase (TRAP) (Fig. 3*B*). Some of these proteins (e.g., CADH2) and additional proteins predominantly expressed in bone cells (e.g., RANKL, Podoplanin, and Cathepsin K) that were not identified by mass spectrometry according to our criteria of inclusion were detected by western blot analysis (Supplemental Fig. S3*A*). Given the identification of ALP by mass spectrometry, we further assessed its enzymatic activity in EV subpopulations. Total ALP activity was consistently higher in sEVs than in lEVs across independent experiments (Supplemental Fig. S3*B*). However, when normalized to vesicle number, lEVs exhibited a higher ALP activity content per million vesicles (Supplemental Fig. S3*C*).

Beyond these common features, our analysis revealed molecular differences between lEV and sEV. KEGG pathway

A

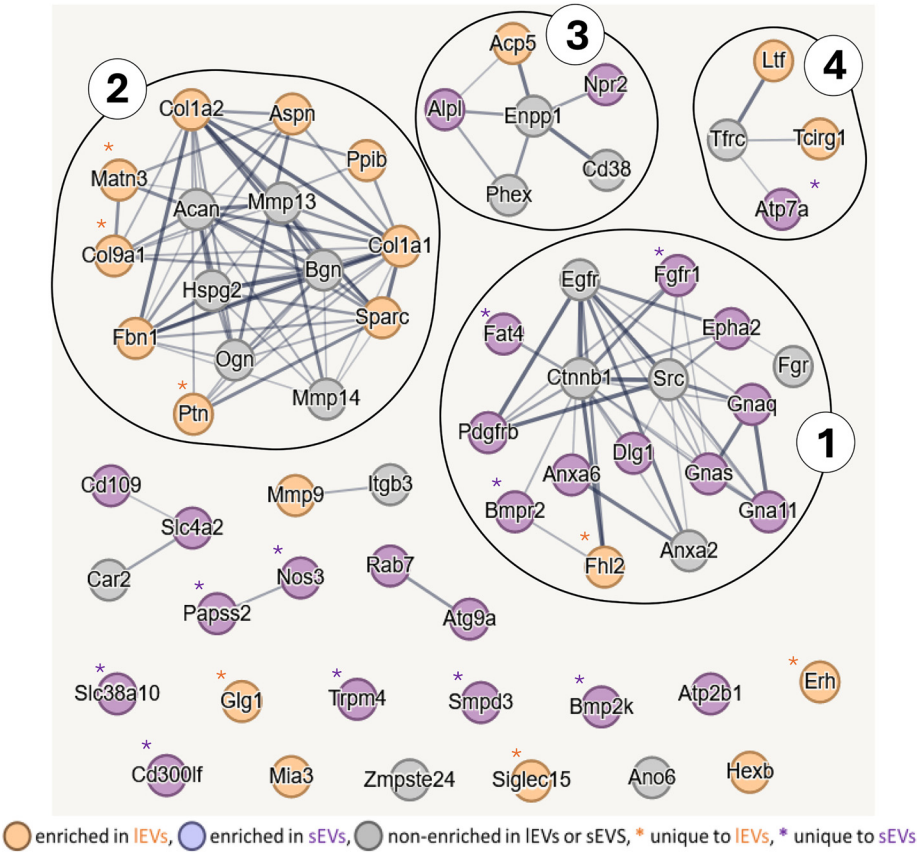

B

1	GO:0060348 : Bone development (p = 4.87e-06)	*Fgr, Dlg1, Epha2, Ctnnb1, Gnas, Gnaq, Src, Fgfr1*, Pdgfrb, Egfr, Flna, Anxa2, Anxa6*
	GO:0060828 : Regulation of canonical Wnt signaling pathway (p = 0.0019)	*Ctnnb1, Src, Egfr, Gnaq*
	GO:000966 : Regulation of signal transduction (p = 1.42e-05)	*Fgr, Dlg1, Epha2, Ctnnb1, Gnas, Gnaq, Src, Egfr, Fgfr1*, Pdgfrb, Flna, Fhl2*, Bmpr2*
	GO:0007167 : Enzyme linked receptor protein signaling pathway (p = 1.71e-07)	*Fgr, Fat4*, Epha2, Ctnnb1, Src, Egfr, Fgfr1*, Pdgfrb, Bmpr*
2	GO:0060348 : Bone development (p = 1.21e-10)	*Mmp14, Sparc, Hspg2, Bgn, Col1a1, Mmp13, Ppib, Col9a1*, Ogn*
	GO:0031012 : Extracellular matrix (p = 8.48e-19)	*Col1a1, Col1a2, Col9a1*, Aspn, Matn3*, Acan, Mmp13, Mmp14, Fbn1, Ptn*, Ogn, Bgn, Hspg2, Sparc*
3	GO:0006793 : Phosphorus metabolic process (p = 0.0213)	*Alpl, Enpp1, Acp5, Npr2, Phex*
	GO:0030282 : Bone mineralization (p = 0.0014)	*Alpl, Enpp1, Phex*
4	GO:0030316 : Osteoclast differentiation (p = 0.0358)	*Tcirg1, Tfrc*

Figure 4. Proteins identified by GO analysis and associated with the skeletal system in lEVs and sEVs. *A*: protein-protein interaction network analysis of common and unique proteins, generated using STRING. Genes encoding proteins most enriched in lEVs are highlighted in orange, those most enriched in sEVs are shown in purple, and those unique to either lEVs or sEVs are marked with an *. *B*: GO terms and KEGG pathways related to the four main clusters. For each, 1–4 terms are listed with *P* values and the associated genes. GO, gene ontology; KEGG, Kyoto Encyclopedia of Genes and Genomes; lEV, large EV population; sEV, small EV population.

analysis showed that proteins exclusive to lEVs are linked to the spliceosome (mmu02040) (Fig. 3*E*). Conversely, proteins unique to sEVs were associated with several pathways, including metabolic pathways (mmu01100), regulation of the actin cytoskeleton (mmu04810), and the vascular endothelial growth factor (VEGF) signaling pathway (mmu04370). Moreover, calcium-binding proteins (e.g., Calpain-6, 45 kDa calcium-binding protein, and soluble calcium-activated nucleotidase 1), phosphatases (e.g., receptor-type tyrosine-protein phosphatase zeta, phosphatase and actin regulator 4, tyrosine protein phosphatase nonreceptor type 13, and 2-phosphoxylose phosphatase 1), and various receptors and G proteins were also found among proteins unique to sEVs (Supplemental Table S3). These results highlight the molecular differences between lEVs and sEVs, which are likely due to their distinct biogenesis pathways and cellular origin.

We focused on proteins associated with skeletal system-related GO terms to identify those relevant to bone biology

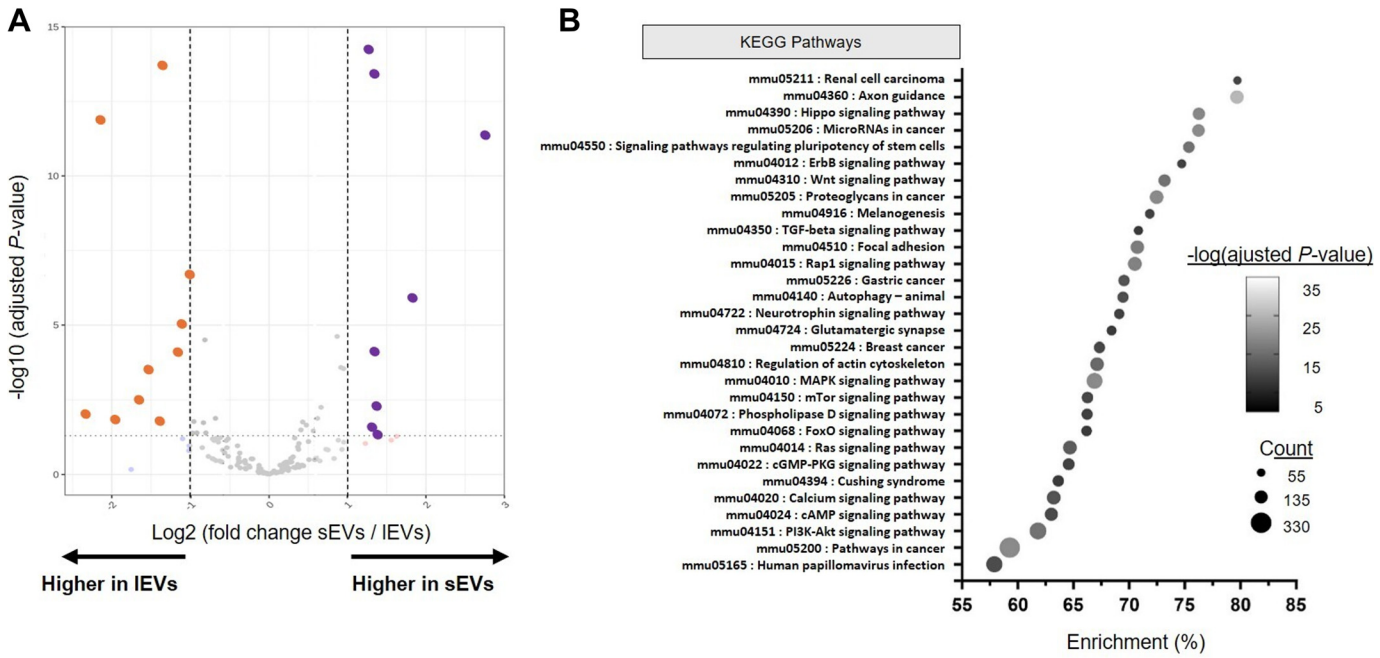

Figure 5. Quantitative miRNA analysis of lEV and sEV subpopulations isolated from bone tissue. *A*: volcano plot showing differentially expressed miRNAs between lEVs and sEVs. The *y*-axis represents the adjusted *P* value (−log10), whereas the *x*-axis shows the fold change between the two EV subpopulations. Vertical lines indicate log2 fold changes of −1 and 1. *B*: KEGG pathway analysis of predicted target genes for 34 miRNAs. The *y*-axis displays the top thirty KEGG pathways, whereas the *x*-axis represents the enrichment level, indicating the percentage of predicted target genes associated with each term. The size of each circle represents the number of predicted target genes. EV, extracellular vesicle; KEGG, Kyoto Encyclopedia of Genes and Genomes; lEV, large EV population; sEV, small EV population.

(Supplemental Table S4). Protein-protein interaction analysis of these proteins (i.e., 45 common, 7 unique to lEVs, and 11 unique to sEVs) revealed four main clusters (Fig. 4, *A* and *B*). These clusters encompassed processes related to cellular signaling, bone development, mineralization, and osteoclast differentiation. Notably, cluster 1 was mostly linked to proteins enriched or unique to sEVs and cluster 2 to proteins enriched or unique to lEVs.

In addition to proteins associated with the skeletal system, some proteins identified in lEVs and sEVs have been found to be related to the nervous and muscular systems, as well as proteins specific to endothelial cells (e.g., CD34, ICAM 1, and VCAM 1) (Supplemental Tables S2 and S3). Several molecules involved in both innate and adaptive immunity, such as complement components (e.g., factor H, C3, C8 α/β) and positive regulators of T cell/B cell activation (e.g., Band 3 anion transport protein, transferrin receptor protein 1, ANXA1, FLOT-1, Semaphorin-7A) were also detected.

To better characterize the molecular cargo of these two EV subpopulations, we also investigated their miRNA content. Small RNA sequencing showed that miRNAs constituted only a small fraction of the total reads, ∼3% for lEVs and 10% for sEVs (Supplemental Fig. S4*A*). PCA analyses demonstrated clear separation between lEV and sEV miRNA profiles as well as high homogeneity between the three replicates (Supplemental Fig. S4*B*). This indicates good reproducibility in the miRNA extraction process and confirms the difference between the two EV subpopulations.

Volcano plot analyses (Fig. 5*A*) revealed 139 miRNAs common to both lEVs and sEVs (Supplemental Table S5), suggesting a shared miRNA landscape across subpopulations, with only limited enrichment of individual miRNAs. KEGG enrichment analysis performed on the 34 miRNAs with an adjusted P value < 0.05 and their predicted target genes identified several pathways implicated in osteogenesis and osteoblast differentiation, including the Hippo (mmu04390), TGF-β (mmu04350), and canonical Wnt (mmu04310) signaling pathways (Fig. 5*B*). Among the predicted target genes listed in Supplemental Table S6, some serve as inducers (e.g., *Wnt* factors, *Tgfb*), whereas others act as inhibitors (e.g., *Axin1*, *Grem2*, *Inhba*, *Nog*, *Ywahq*, *Ppp2r2d*, *Ppp2cb*, *Ppp2ca*, and *Sost*), suggesting that these miRNAs could modulate these pathways either positively or negatively.

Although no miRNAs were found to be uniquely associated with either subpopulation, the presence of osteogenesis-related miRNAs in both lEVs and sEVs supports their potential involvement in the regulation of osteogenic signaling mechanisms. These findings, consistent and complementary to proteomic data, underline the functional relevance of EVs in skeletal biology.

Analysis of the Osteogenic Potential of the Two EV Subpopulations

To evaluate EVs with potential functional roles, it was critical to assess their cellular uptake. We assessed the internalization of the two bone-derived EV subpopulations by ST2 (Fig. 6*A*) and MC3T3-E1 (Fig. 6*B*) cells. The EVs were prelabeled with a green fluorescent dye, incubated with the cells for 4 h, and then visualized using confocal microscopy. The results showed that the green fluorescence was observed inside cells, indicating successful internalization of both lEVs and sEVs. The fluorescence was predominantly localized to the perinuclear region of the cells.

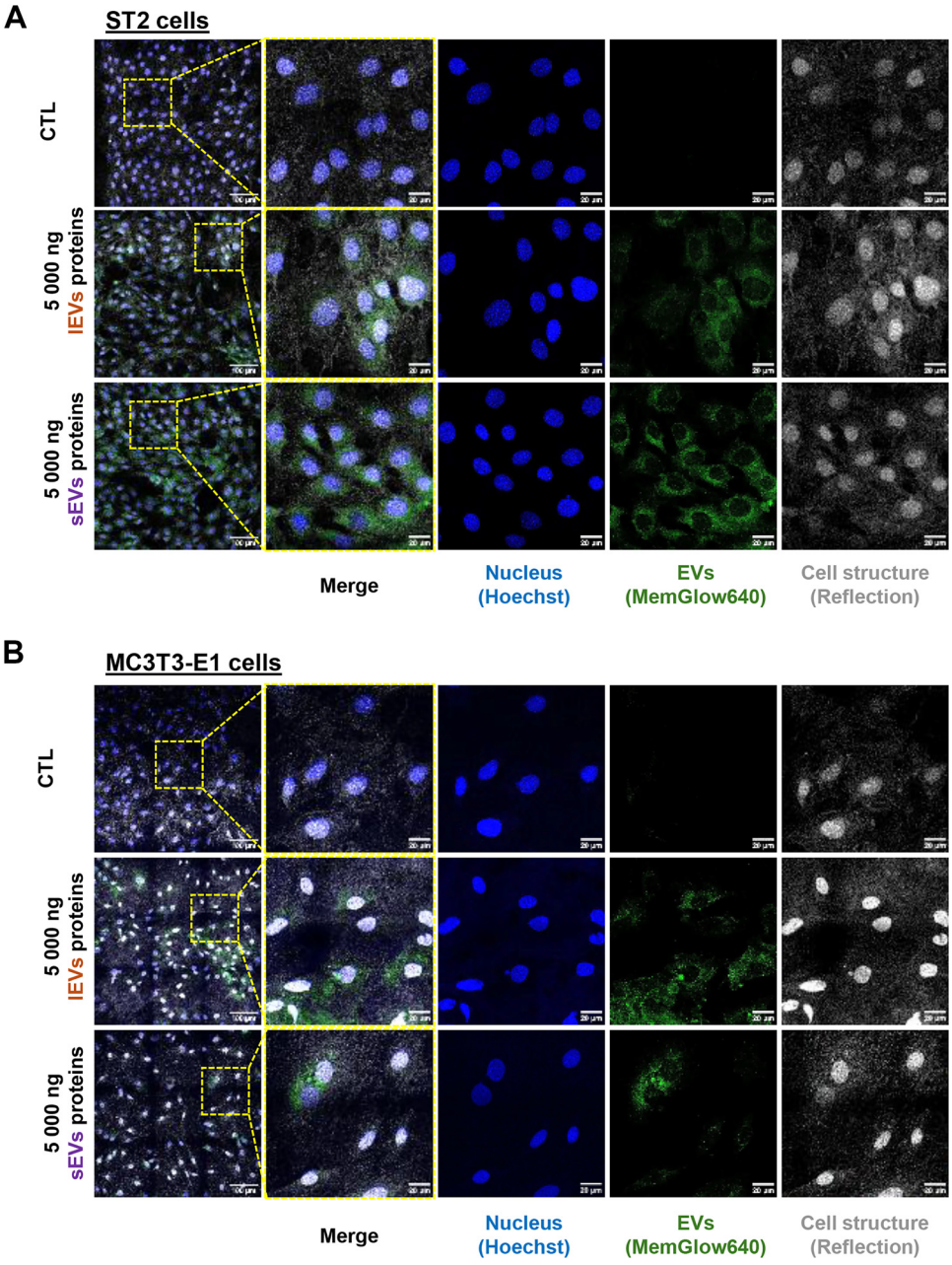

Figure 6. Cellular uptake of lEVs and sEVs. Internalization of EVs labeled with MemGlow 640 was examined in stromal cells (ST2) (*A*) and preosteoblastic cells (MC3T3-E1) (*B*) after 4 h of incubation. The experiments used 5,000 ng of lEVs proteins (equivalent to 3.76×10^8 EVs) and 5,000 ng of sEVs proteins (equivalent to 3×10^9 EVs). Nuclei were stained with Hoechst, and cell structure was visualized by reflection. Control condition (CTL) corresponds to cells incubated with MemGlow 640 in PBS. Reflection images were used to visualize the shape and structure of the cells. The dataset includes representative images from 6 and 3 experiments involving lEVs and sEVs with ST2 cells, and 3 and 1 experiments involving lEVs and sEVs with MC3T3-E1 cells. EV, extracellular vesicle; lEV, large EV population; PBS, phosphate-buffered saline; sEV, small EV population.

The osteogenic potential of lEVs and sEVs that was suggested by proteomic and small RNA-seq analysis, was assessed with ST2 stromal cells. These bone marrow-derived cells represent a relevant model for investigating early stages of osteoblastic differentiation, as they are not yet engaged into the osteoblastic lineage and can differentiate into osteoblasts upon appropriate stimulation. To evaluate the commitment of the ST2 cells into the osteoblastic lineage, ALP activity and osterix (*Osx*) gene expression were assessed. At the higher dose, lEVs exhibited a transient but substantial and significant effect on ALP activity. Specifically, lEVs at the higher dose induced a tenfold increase in ALP activity on *day 1*, and a twofold increase on *day 3*. However, there was no significant change in osterix (*Osx*), an early marker of osteoblast differentiation, and osteocalcin (*Ocn*) expression, a marker of mature osteoblast (Fig. 7*A*). Similar results were obtained for the expression of two other late markers, Osteopontin (*Opn*) and Bone sialoprotein (*Bsp*) (data not shown). In contrast, sEVs had no significant effect on ALP activity, *Osx* and *Ocn* expression in ST2 cells (Fig. 7*B*).

The MC3T3-E1 preosteoblastic cell line and primary osteoblasts (POB) isolated from newborn mouse calvaria were proven to be more effective than ST2 for assessing the effect of the EVs subpopulations on osteoblastic activity, probably because both are already committed to the osteoblastic lineage. This makes them better suited for evaluating the later stages of osteogenic differentiation, including matrix production and mineralization. Mineralized nodule formation assay was conducted with POBs in the presence or absence of sEVs from two independent productions at X10 dose. The assay suggested that sEVs partially restored the ability of POBs to form mineralized nodules in vitro, which was dramatically

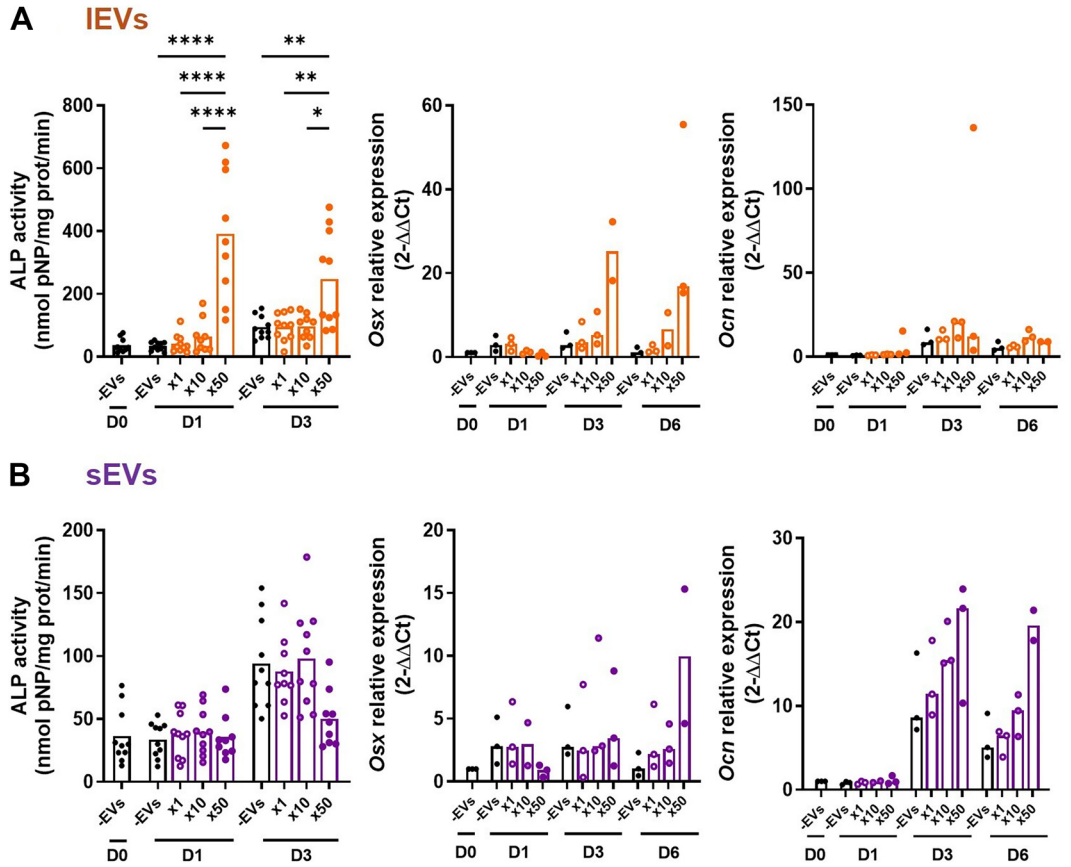

Figure 7. Effect of lEVs and sEVs on osteoblastic differentiation. *A* and *B*: the effect of lEVs and sEVs, respectively, on ALP activity on *days 0* (D0), *1* (D1), and *3* (D3) and on the gene expression of early (Osterix, *Osx*) and late (Osteocalcin, *Ocn*) osteoblastic markers in ST2 cells after osteogenic treatment on *days 0* (D0), *1* (D1), *3* (D3), and *6* (D6). Results are presented relative to the expression levels of −EVs at *day 0* control condition. EVs were isolated from pools of 30–40 hindlimbs of 8-wk-old SWISS male mice for each independent experiment. The EV doses are indicated as follows: X1 = 4.2×10^7 EVs/cm^2; X10 and X50 correspond to 10 and 50 times the X1 dose, respectively. Cells treated with PBS served as the −EVs control. Statistical significance was determined by one-way ANOVA followed by Tukey's post hoc test (*$P < 0.05$; **$P < 0.005$; ****$P < 0.0001$) for ALP activity. Scatter plots with bars at the mean and individual values are shown. For gene expression, the nonparametric Kruskal–Wallis test followed by Dunn's post hoc test was used and individual values and a line at the median are shown ($N = 9$ or 10, $n = 4$ or 5 for ALP activity, $N = 3$, $n = 3$ for gene expression). ALP, alkaline phosphatase; EV, extracellular vesicle; lEV, large EV population; PBS, phosphate-buffered saline; sEV, small EV population.

impaired when ultracentrifuged EV-depleted serum was used (Fig. 8*A*). Specifically, densitometric quantification showed a fourfold reduction in alizarin red staining with EV-depleted serum, and the addition of sEVs to the EV-depleted serum induced an increase in alizarin staining (Fig. 8*B*). However, although sEVs addition seemed to induce an increase in nodules formation at *day 21* in primary osteoblasts, no effect on ALP activity could be observed when sEVs were added to MC3T3-E1 cells culture at *days 1* and *3* (Fig. 8*C*).

In these culture conditions, lEVs had no effect on mineralized nodules formation on primary osteoblasts (data not shown).

Taken together, these in vitro observations indicate distinct effects of the two EV subpopulations on stromal cell differentiation and osteoblastic activity and suggest a complementary role in osteogenesis.

DISCUSSION

To characterize the subpopulations of EVs present in mouse long bones, identify their protein and microRNA cargos, and initiate the evaluation of their osteogenic properties, we extracted EVs directly from bone tissue. The isolation of EVs from whole bone represented a major technical challenge, particularly due to the density of bone tissue. Considering the complexity of its cellular composition, this approach was favored over isolation from cell culture supernatants to ensure the analysis of natural EVs, thereby minimizing potential biases introduced by artificial culture conditions and stressors commonly used to enhance EV yield. Furthermore, isolating EVs from fresh tissue helped limit cell death and prevented the risk of excessive coisolation of apoptotic bodies (46). Our proteomic analysis supported the robustness of this strategy, since only a few proteins associated with cell death and apoptotic processes were detected in lEVs, and proteins linked to apoptotic cell clearance were found in sEVs. As opposed to EVs from cultured bone cells, which dominate the existing literature, EV isolation directly from bone tissue has been successfully reported only in a small number of studies (33, 47, 48). Existing methods rely mainly on ultracentrifugation, often associated with enzymatic digestion (47, 48), which can alter EV content. Although complementary techniques such as size exclusion chromatography (SEC) can effectively remove contaminants,

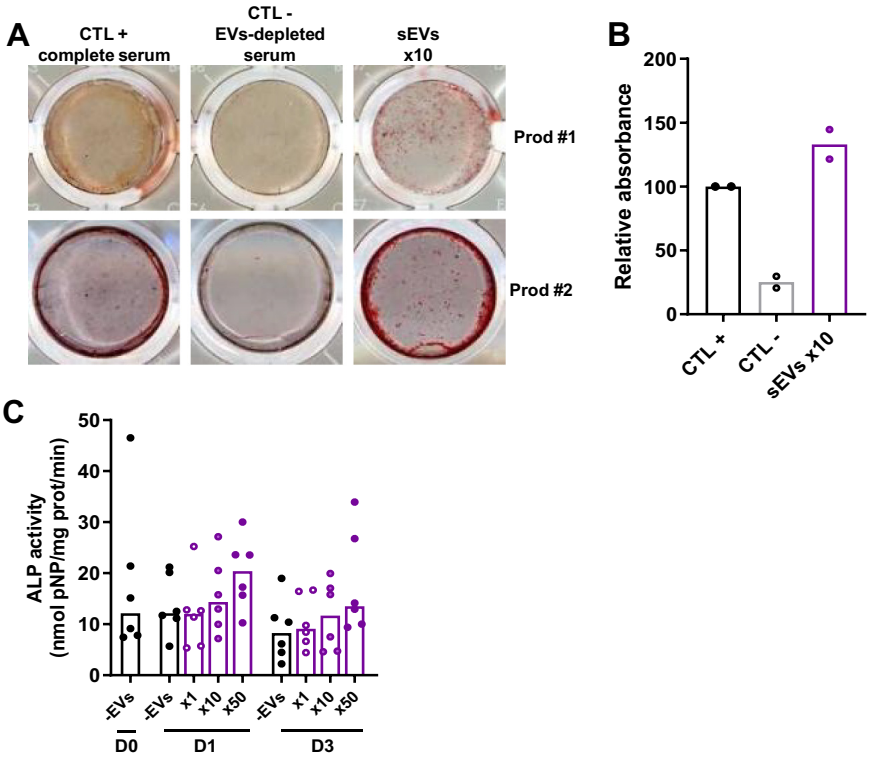

Figure 8. Effect of sEVs on osteoblast activity. *A*: mineralized nodule formation assay was assessed after 3 wk using Alizarin Red S staining in primary osteoblasts (POBs) isolated from the calvaria of 2–4-day-old newborn mice. Cells were cultured in osteogenic media containing either 10% FBS (CTL+ complete serum), 10% EV-depleted FBS (CTL−), or 3.57×10^8 sEVs/cm^2 (corresponding to the X10 dose). Media and sEVs were replaced twice weekly. Results from two independent preparations of sEVs, isolated from pools of 40–50 hindlimbs of 8-wk-old SWISS male mice, are presented. *B*: densitometric quantification of Alizarin Red staining is shown, with results expressed relative to the positive control (CTL+). Data were normalized to CTL+ condition. Individual values and a line at mean are shown, $N = 2$. *C*: ALP activity was measured in the MC3T3-E1 cell line at *days 0* (D0), *1* (D1), and *3* (D3). Cells treated with PBS served as the −EVs control. The EV doses are indicated as follows: X1 = 4.2×10^7 EVs/cm^2; X10 corresponds to 10 times the 1 dose. Statistical significance was determined by the nonparametric Kruskal–Wallis test followed by Dunn's post hoc test. Individual values and a line at the median are shown ($N = 6$, $n = 4$ or 5). EVs were isolated from pools of 30 hindlimbs from 8-wk-old SWISS male mice. ALP, alkaline phosphatase; CTL, control; EV, extracellular vesicle; FBS, fetal bovine serum; PBS, phosphate-buffered saline; sEV, small EV population.

SEC significantly reduces particle yield (49). Instead, we opted for an ultracentrifugation protocol incorporating a sucrose cushion, a modification shown by Gupta et al. (50) to improves EV purity without sacrificing yield, therefore minimizing the number of animals sacrificed.

Given the potential contamination by intracellular vesicles released from ruptured cells or circulating EVs, we meticulously analyzed the physical and biological characteristics of bone cell-derived vesicles. STEM confirmed the typical cup-shaped morphology of EVs, and immunoblotting and proteomic analysis demonstrated the presence of canonical EV markers in both large (lEV) and small (sEV) subpopulations, supporting their identity as EVs. The detection of common vesicular markers across both subpopulations was expected, given the lack of specific markers in the literature to distinguish between EV subtypes (6).

Altogether, these findings confirm the successful and reproducible isolation of two EV subpopulations from mouse bone tissue.

Our physicochemical characterization and cargo identification revealed that both lEVs and sEVs are intrinsically heterogeneous, with substantial overlap in their respective cargos, ~90% of proteins being shared between the both. Despite this overlap, and although the presence of contaminants in our EV preparations cannot be entirely ruled out, the two subpopulations exhibited partially distinct molecular profiles. For example, although recent research on bone- or osteocyte-derived EVs has primarily focused on exosomes (13), in line with broader trends in EV studies (51), our data provide evidence for the existence of functionally active lEVs subpopulation within bone tissue. This population shows distinct physicochemical properties and carries unique proteins not detected in sEVs, suggesting that these two EVs subpopulations may have distinct roles or functions, possibly contributing to bone homeostasis.

Our findings corroborate previous studies that identified proteins in EVs derived from various cellular organelles, such as the nucleus/nucleoplasm (52, 53), the Golgi apparatus (54), the endoplasmic reticulum (46), and the mitochondria (55, 56). This may result from organelle transfer via lEVs or from intracellular vesicle crosstalk during EV biogenesis, especially in sEVs (57). Since the mechanisms by which proteins and microRNAs are sorted into EVs are not yet fully understood and are likely to vary (58), the presence of organelle-specific markers likely reflects the functional diversity of EVs rather than only contamination, as previously reported in brain-derived EVs (59).

Since sEVs were prepared using a protocol initially designed for extracting MVs from bone, it is plausible that MVs were coisolated with the sEV fraction. MVs, secreted by osteoblasts and localized in the bone matrix (60), typically do not undergo cellular internalization; however, they play a critical role in ECM mineralization due to their high ALP content, an enzyme essential for initiating this process (61). Despite their established functions, there is ongoing debate regarding the classification of MVs as EVs (28). Recent studies, however, have highlighted differences in size, protein composition, and function between MVs and EVs derived from osteoblastic cell lines in vitro, suggesting that these vesicle types have unique roles and characteristics (30). Supporting this view, the hydroxyapatite crystals, usually observed in MVs (61), were not detected within sEVs in our STEM observations. Thus, sEVs isolated from bone appear to be fundamentally different from MVs, thereby reinforcing the idea that they represent independent EV subpopulations with separate and complementary physiological functions. Therefore, the presence of MVs in our sEV

subpopulation alone cannot account for the partial restoration of the mineralizing nodule formation capacity of POBs, which highlights the role of sEVs.

Given the diversity of cell types within bone tissue, accurately pinpointing the origins of bone-derived EVs poses a significant challenge. In contrast to cell culture, where cell numbers can be quantified, tissue samples do not offer direct and easy access to their cellular composition. To determine the overall cellular origins of EVs extracted from bone tissue, the identification of specific markers becomes essential. Our proteomic data revealed markers associated with osteocytes, osteoblasts, and osteoclasts, indicating that EVs released by all three lineages were present, albeit in undetermined proportions. Nevertheless, the predominance of osteoblast/osteocyte markers suggests that most EVs originated from that lineage.

Furthermore, not all bone cells release EVs simultaneously or in equal quantities. The protein content of these EVs reflects the variability in cellular responses to various stimuli, such as mechanical stress and hypoxia. This heterogeneity likely reflects the dynamic and responsive nature of bone tissue to its mechanical and biochemical environment. Our proteomic and small RNA-seq analyses indicate that a portion of the bone-extracted EVs originates from osteocytes, which is consistent with their prevalence as the most abundant cell type in bone. We confirmed the presence in both EV subpopulations of podoplanin, a protein widely present in young embedded osteocytes that is involved in dendritic formation (3), and PHEX, a protein highly expressed in osteocytes that regulates biomineralization and mineral metabolism (3). Peptides corresponding to other proteins highly expressed in osteocytes, such as Dentin matrix acidic phosphoprotein 1 (DMP1) and Matrix extracellular phosphoglycoprotein (MEPE), were also detected, but their number did not meet our criteria for analysis inclusion. It is crucial to acknowledge the heterogeneity of osteocytes; their functionality and responses can vary significantly based on their location within the osteocyte network and the bone microstructure, which directly influences the mechanical stimuli they experience, and likely contributes to the variability in their EV cargo. Vaughan et al. (62) have observed that only a subset of osteocytes acts as mechanoreceptors. Therefore, it is not surprising that not all osteocytes release EVs in response to mechanical stimuli. Similarly, biochemical signals may not uniformly affect all osteocytes at once (63). This introduces a limitation in interpreting the EV origin purely based on markers, as it cannot distinguish between these different states.

Interestingly, our analysis also revealed proteins related to neuronal functions, such as synapse and axon guidance, as noted by Youlten et al. (64) in osteocytes. Some of these genes were also highlighted in a transcriptomic study by Paic et al. (65). The identified proteins are essential for establishing the osteocyte network (66). Our analysis revealed the presence of Semaphorin-7A and Plexin-B2, molecules initially recognized for their roles in axonal guidance, that have also been associated with the promotion of osteoblast differentiation (67, 68). Their presence in bone-derived EVs supports the hypothesis that osteocyte-derived EVs carry bioactive factors that positively influence the osteoblast-osteocyte lineage, facilitating the differentiation of osteocyte precursors.

Several miRNAs have been detected in osteocyte cell lines and primary cells (69) or associated with their EVs (18). Among the most frequently reported miRNAs, we identified several in our lEV and sEV subpopulations, including the miR-23 cluster, miR-29b-3p, miR-3473b/e, and miR-145-5p. These miRNAs are known to influence the osteoblast-osteocyte lineage by either suppressing osteoblast differentiation, impairing osteocyte function, or promoting the differentiation of both osteoblasts and osteocytes. Furthermore, these miRNAs are often implicated as downstream effectors of mechanical stimulation in osteocytes (19, 70). The consistency of these miRNA profiles in our EV subtypes confirms previously observed osteocyte-EV signatures. Other miRNAs previously described in EVs derived from osteocyte-like cell lines, such as MLO-Y4 and OCY454, were also detected in our small RNA-seq analysis but were excluded from further analysis as P values were >0.05. Notably, and miR-218, found in OCY454-derived exosomes and known to induce osteoblastogenesis through the canonical Wnt pathway (17), was among those detected.

In addition, several studies have highlighted the multifaceted roles of osteoblast-derived EVs in osteogenesis and in the induction of osteoclast resorption (23, 71). In line with this, we detected miRNAs known to be enriched in osteoblast-derived EVs, including members of the let-7 family, miR-125b, miR-29a-3p, and miR-23a/23b-3p. (72). In particular, miR-125b, which was enriched in sEVs in our study, was previously shown to regulate osteoblast differentiation by targeting Cbfβ, a protein that forms heterodimers with Runx proteins, and BMPR1b in MSCs (73, 74). Furthermore, miR-143-3p, known to inhibit bone formation and promote osteoclastogenesis by targeting Cbfβ (71), was present in both lEVs and sEVs in our analysis.

Proteins and miRNAs widely described in osteoclasts (75, 76) were also detected in bone-derived EVs, including cathepsin K (by western blot), and matrix metallopeptidase 9 (MMP9), TRAP, the subunit of type V proton ATPase, and transferrin receptor protein 1 (through proteomic analysis). MMP9 and TRAP were exclusively found in lEVs. Furthermore, miR-214, a miRNA previously associated with osteoclast-derived exosomes and known to inhibit osteoblast function (20, 22) while promoting osteoclast differentiation (77), was identified, although its adjusted P value exceeded 0.05.

Overall, these results support the multilineage origin of bone EVs, with a main contribution from osteocyte and osteoblast. It highlights the complex and dynamic nature of bone EVs and their cargo, which likely reflects both the cellular diversity of bone tissue and the functional heterogeneity of EV-producing cells in response to environmental cues.

As we extracted EVs from whole bone, an organ in which vascularization is essential for development and regeneration, we anticipated detecting proteins specific to endothelial cells. However, we identified only a limited number of endothelial markers. This low detection likely reflects the low vascular volume density (~0.13 %) in the midfemoral diaphysis (78), and therefore may represent a sampling limitation rather than a biological absence. By contrast, the detection of several complement components and positive regulators of T cell/B cell activation aligns with the emerging concept of osteoimmunology, whereby EVs contribute to immune and bone cell interactions (79). A recent study by Zhang et al. (48) supports this view, having identified immune-related molecules in exosomes isolated from cortical bone through proteomic and

transcriptomic analyses. Our findings further support this novel hypothesis of a potential novel pathway for mutual regulation between the skeleton and the immune system.

Large and small EVs contain proteins and microRNAs that suggest a potential role in osteogenic activity and in regulating bone remodeling to maintain bone health. We evaluated their ability to induce cell differentiation using the stromal ST2 cell line, to increase cell activity using the preosteoblastic MC3T3-E1 cell line, and to induce mineralization using primary osteoblasts from calvaria. Both lEVs and sEVs were internalized by the ST2 and MC3T3-E1 cell lines, likely through natural cellular uptake mechanisms, although other pathways involving specific ligands or receptors on the surfaces of EVs and cells cannot be ruled out (80).

Under our experimental conditions, only lEVs significantly enhanced the activity of ALP, an early marker of osteoblast differentiation, in the stromal ST2 cell line. This suggests that lEVs may promote osteoblastic commitment of stromal progenitors. Notably, this effect was transient, likely due to a single administration of EVs, with maximal activity observed shortly after addition. This experimental setup, although informative, does not reflect the sustained exposure that may occur in vivo and should be considered a limitation of our in vitro analysis. Several key components within lEVs may contribute to the observed pro-osteogenic effect. Among them, pleiotrophin (PTN), an angiogenic factor known to enhance osteoblast differentiation (81), and four and a half LIM domains 2 (FHL-2), a multifunctional adaptor protein involved in bone regulation (82) and the canonical Wnt/β-catenin pathway in osteoblasts (83), are of particular interest. Enhancer of rudimentary homolog, though less characterized in bone, has been implicated in transcriptional regulation and cell cycle control (84). In addition, lEVs are enriched with osteogenesis-related miRNAs, including miR-15b-5p, which targets smad ubiquitination regulatory factor 1 (SMURF1), a protein that degrades Runx2 and inhibits transforming growth factor β/bone morphogenetic protein (TGF-β/BMP) signaling pathways (85). Other relevant miRNAs, such as miR-29a-3p and miR-128-3p, are known to enhance the Wnt signaling pathway (86–88). Notably, both proteomic and miRNA analyses revealed that lEVs are enriched with bone matrix components, such as Type I collagen, Fibrillin-1, and Asporin, as well as proteins involved in bone matrix organization, including Osteonectin and PTN. Together with the presence of miR-29, these cargo elements may contribute to the early phases of osteoblast differentiation, supporting the transition from stromal commitment (89) to matrix production, possibly through the activation of osteogenic pathways such as Wnt and BMP.

In contrast, sEVs do not affect *Osx* and *Ocn* gene expression in ST2 cells or on ALP activity in ST2 and MC3T3-E1 cells. But sEVs partially restored the ability of primary osteoblasts to form mineralized nodules under EV-depleted conditions, possibly due to the presence of proteins specifically associated with the process of bone matrix mineralization, such as plasma membrane calcium-transporting ATPase 1 (ATP2B1) (90) and bifunctional 3′-phosphoadenosine 5′-phosphosulfate synthase 2 (PAPSS2) (91), several phosphatases, and various receptors and G proteins.

Altogether, our results underscore a functional complementarity between lEVs and sEVs. Our data highlight the osteoinductive potential of lEVs and their ability to prime stromal progenitors toward osteoblast differentiation. Conversely, sEVs seems to contribute to osteogenesis through distinct mechanisms.

In conclusion, in recent years, there has been a surge of interest in using MSC-derived EVs for bone tissue engineering and regenerative medicine. Simultaneously, researchers have concentrated on identifying the cargo of EVs from various cellular origins that are integral to bone homeostasis and regeneration (92, 93). This study primarily aimed to extract, characterize, and start evaluating the osteogenic properties of bone-derived EV subpopulations in vitro.

Despite the challenges associated with isolating EVs from hard bone tissue, we successfully established a reproducible protocol for extraction. For the first time, we isolated and separated EVs extracted from bone tissue according to size by ultracentrifugation into two EV subpopulations, lEVs and sEVs, each exhibiting distinct effects on stromal and preosteoblastic cell lines in vitro. Our comprehensive proteomic and miRNA analyses suggest that specific cargo within these EVs may replicate some aspects of the functions of osteoclasts, osteoblasts, and osteocytes.

This work represents a significant step toward the functional characterization of bone EVs and provides a strong foundation for future studies aimed at fully elucidating their complex mechanisms of action. Although the osteogenic assays were conducted in vitro under controlled conditions, which differ from the in vivo dynamic environment, they offer valuable insights into the potential of these EVs and highlight the importance of exploring them further. Importantly, these findings open promising avenues for the development of targeted EV-based strategies to enhance bone regeneration.

ETHICAL APPROVALS

This study was conducted in compliance with French and European regulations regarding the care and protection of laboratory animals (EC Directive 86/609 and French Law 2001-486, enacted on June 6, 2001).

DATA AVAILABILITY

All data supporting the findings of this study are available within the article and in the Supplemental Material. The mass spectrometry proteomics raw data have been deposited in the ProteomeXchange Consortium via the PRIDE (94) partner repository, with the dataset identifier PXD 047653. The small RNA-Seq raw data have been deposited in the Gene Expression Omnibus (GEO) with dataset identifier GSE250170.

SUPPLEMENTAL MATERIAL

Supplemental Figs. S1–S4: https://doi.org/10.6084/m9.figshare.30041860.

Supplemental Tables S1–S6: https://doi.org/10.6084/m9.figshare.30042196.

ACKNOWLEDGMENTS

The authors thank the IRS-UN UTE platform from Unité Mixte de Service (UMS) BioCore [Institut national de la santé et de la recherche médicale (Inserm) US016 - Unité d'Appui et de Recherche

(UAR) Centre National de la Recherche Scientfique (CNRS) 3556] and Nantes Université as well as the SC3M platform from the Inserm (/NU/ONIRIS UMR1229 Regenerative Medicine and Skeleton (RMeS) Laboratory and SFR François Bonamy-UMS 016. The authors also acknowledge the Infrastructures en Biologie, Santé et Agronomie (IBiSA) MicroPICell facility (Biogenouest), a member of the national infrastructure France-Bioimaging, supported by the French National Research Agency (ANR-10-INBS-04). Special thanks are extended to the GENOM'IC sequencing facility of the Institut Cochin (INSERM U1016, Paris, France) for assistance with the small RNA-Seq analysis. The authors are grateful to Julie Gavard [Centre de Recherche en Cancérologie et Immunologie Intégrée Nantes Angers (CRCI^{2}NA), Research Cancer Center, Inserm U1307, CNRS UMR6075] and Olivier Blanc-Brude [Inserm U970, Center de Recherche Cardiovasculaire (PARCC)] for valuable discussions and insights.

GRANTS

This work was funded by the Agence Nationale de la Recherche (ANR) under Grant ANR-20-CE18-0015-01 and the Société Française de Rhumatologie (SFR) under Grant SFR-2018-2019-4959. Additional support was provided by core funding from the Institut National de la Santé et de la Recherche Médicale (Inserm) and Nantes Université allocated to the Regenerative Medicine and Skeleton Laboratory (UMR 1229 RMeS). Mass spectrometry proteomics analysis was financially supported by "la Région Île-de-France" (N°EX061034) and ITMO Cancer of Aviesan and INCa, with funds administered by Inserm (N°21CQ016-00).

DISCLOSURES

No conflicts of interest, financial or otherwise, are declared by the authors.

AUTHOR CONTRIBUTIONS

F.B., L.E., A.G., and V.G. conceived and designed research; F.B., L.E., M.A., S.T., J.V., L.D.B., G.A.-G., F.D., D.L., A.G., and V.G. performed experiments; F.B., L.E., F.D., D.L., A.G., and V.G. analyzed data; F.B., L.E., F.D., D.L., A.G., and V.G. interpreted results of experiments; F.B., L.E., F.D., A.G., and V.G. prepared figures; F.B., L.E., F.D., D.L., A.G., and V.G. drafted manuscript; F.B., L.E., A.G., and V.G. edited and revised manuscript; F.B., L.E., M.A., S.T., J.V., L.D.B., G.A.-G., F.D., D.L., P.W., A.G., and V.G. approved final version of manuscript.

REFERENCES

1. **Kim J-M**, **Lin C**, **Stavre Z**, **Greenblatt MB**, **Shim J-H.** Osteoblast-osteoclast communication and bone homeostasis. *Cells* 9: 2073, 2020. doi:10.3390/cells9092073.
2. **Bonewald LF.** The amazing osteocyte. *J Bone Miner Res* 26: 229–238, 2011. doi:10.1002/jbmr.320.
3. **Delgado-Calle J**, **Bellido T.** The osteocyte as a signaling cell. *Physiol Rev* 102: 379–410, 2022. doi:10.1152/physrev.00043.2020.
4. **Buenzli PR**, **Sims NA.** Quantifying the osteocyte network in the human skeleton. *Bone* 75: 144–150, 2015. doi:10.1016/j.bone.2015.02.016.
5. **Dallas SL**, **Prideaux M**, **Bonewald LF.** The osteocyte: an endocrine cell … and more. *Endocr Rev* 34: 658–690, 2013. doi:10.1210/er.2012-1026.
6. **Vig S**, **Fernandes MH.** Bone cell exosomes and emerging strategies in bone engineering. *Biomedicines* 10: 767, 2022. doi:10.3390/biomedicines10040767.
7. **Jiao Y**, **Liu Y**, **Du J**, **Xu J**, **Luo Z**, **Liu Y**, **Guo L.** Advances in the study of extracellular vesicles for bone regeneration. *Int J Mol Sci* 25: 3480, 2024. doi:10.3390/ijms25063480.
8. **Welsh JA**, **Goberdhan DCI**, **O'Driscoll L**, **Buzas EI**, **Blenkiron C**, **Bussolati B et al.** Minimal information for studies of extracellular vesicles (MISEV2023): from basic to advanced approaches. *J Extracell Vesicles* 13: e12404, 2024 [Erratum in *J Extracell Vesicles* 13: e12451. 2024]. doi:10.1002/jev2.12404.
9. **Tkach M**, **Théry C.** Communication by extracellular vesicles: where we are and where we need to go. *Cell* 164: 1226–1232, 2016. doi:10.1016/j.cell.2016.01.043.
10. **van Niel G**, **D'Angelo G**, **Raposo G.** Shedding light on the cell biology of extracellular vesicles. *Nat Rev Mol Cell Biol* 19: 213–228, 2018. doi:10.1038/nrm.2017.125.
11. **Yáñez MM**, **Siljander PRM**, **Andreu Z**, **Zavec AB**, **Borràs FE**, **Buzas EI**, **et al.** Biological properties of extracellular vesicles and their physiological functions. *J Extracell Vesicles* 4: 27066, 2015. doi:10.3402/jev.v4.27066.
12. **Pitt JM**, **Kroemer G**, **Zitvogel L.** Extracellular vesicles: masters of intercellular communication and potential clinical interventions. *J Clin Invest* 126: 1139–1143, 2016. doi:10.1172/JCI87316.
13. **Wang Z**, **Zhao Z**, **Gao B**, **Zhang L.** Exosome mediated biological functions within skeletal microenvironment. *Front Bioeng Biotechnol* 10: 953916, 2022. doi:10.3389/fbioe.2022.953916.
14. **Qin Y**, **Wang L**, **Gao Z**, **Chen G**, **Zhang C.** Bone marrow stromal/stem cell-derived extracellular vesicles regulate osteoblast activity and differentiation in vitro and promote bone regeneration in vivo. *Sci Rep* 6: 21961, 2016. doi:10.1038/srep21961.
15. **Deng L**, **Wang Y**, **Peng Y**, **Wu Y**, **Ding Y**, **Jiang Y**, **Shen Z**, **Fu Q.** Osteoblast-derived microvesicles: a novel mechanism for communication between osteoblasts and osteoclasts. *Bone* 79: 37–42, 2015. doi:10.1016/J.BONE.2015.05.022.
16. **Narayanan K**, **Kumar S**, **Padmanabhan P**, **Gulyas B**, **Wan ACA**, **Rajendran VM.** Lineage-specific exosomes could override extracellular matrix mediated human mesenchymal stem cell differentiation. *Biomaterials* 182: 312–322, 2018. doi:10.1016/j.biomaterials.2018.08.027.
17. **Qin Y**, **Peng Y**, **Zhao W**, **Pan J**, **Ksiezak-Reding H**, **Cardozo C**, **Wu Y**, **Pajevic PD**, **Bonewald LF**, **Bauman WA**, **Qin W.** Myostatin inhibits osteoblastic differentiation by suppressing osteocyte-derived exosomal microRNA-218: a novel mechanism in muscle-bone communication. *J Biol Chem* 292: 11021–11033, 2017. doi:10.1074/jbc.M116.770941.
18. **Sato M**, **Suzuki T**, **Kawano M**, **Tamura M.** Circulating osteocyte-derived exosomes contain miRNAs which are enriched in exosomes from MLO-Y4 cells. *Biomed Rep* 6: 223–231, 2017. doi:10.3892/br.2016.824.
19. **Eichholz KF**, **Woods I**, **Riffault M**, **Johnson GP**, **Corrigan M**, **Lowry MC**, **Shen N**, **Labour M-N**, **Wynne K**, **O'Driscoll L**, **Hoey DA.** Human bone marrow stem/stromal cell osteogenesis is regulated via mechanically activated osteocyte-derived extracellular vesicles. *Stem Cells Transl Med* 9: 1431–1447, 2020. doi:10.1002/sctm.19-0405.
20. **Sun W**, **Zhao C**, **Li Y**, **Wang L**, **Nie G**, **Peng J**, **Wang A**, **Zhang P**, **Tian W**, **Li Q**, **Song J**, **Wang C**, **Xu X**, **Tian Y**, **Zhao D**, **Xu Z**, **Zhong G**, **Han B**, **Ling S**, **Chang Y-Z**, **Li Y.** Osteoclast-derived microRNA-containing exosomes selectively inhibit osteoblast activity. *Cell Discov* 2: 16015, 2016. doi:10.1038/celldisc.2016.15.
21. **Huynh N**, **Vonmoss L**, **Smith D**, **Rahman I**, **Felemban MF**, **Zuo J**, **Rody WJ**, **McHugh KP**, **Holliday LS.** Characterization of regulatory extracellular vesicles from osteoclasts. *J Dent Res* 95: 673–679, 2016. doi:10.1177/0022034516633189.
22. **Li D**, **Liu J**, **Guo B**, **Liang C**, **Dang L**, **Lu C**, **He X**, **Cheung HY**, **Xu L**, **Lu C**, **He B**, **Liu B**, **Shaikh AB**, **Li F**, **Wang L**, **Yang Z**, **Au DW**, **Peng S**, **Zhang Z**, **Zhang BT**, **Pan X**, **Qian A**, **Shang P**, **Xiao L**, **Jiang B**, **Wong CK**, **Xu J**, **Bian Z**, **Liang Z**, **Guo DA**, **Zhu H**, **Tan W**, **Lu A**, **Zhang G.** Osteoclast-derived exosomal miR-214-3p inhibits osteoblastic bone formation. *Nat Commun* 7: 10872, 2016 [Erratum in *Nat Commun* 16: 5348. 2025]. doi:10.1038/ncomms10872.
23. **Liu M**, **Sun Y**, **Zhang Q.** Emerging role of extracellular vesicles in bone remodeling. *J Dent Res* 97: 859–868, 2018. doi:10.1177/0022034518764411.
24. **Tao S-C**, **Guo S-C.** Extracellular vesicles in bone: "dogrobbers" in the "eternal battle field. *Cell Commun Signal* 17: 6, 2019. doi:10.1186/s12964-019-0319-5.
25. **Qi X**, **Zhang J**, **Yuan H**, **Xu Z**, **Li Q**, **Niu X**, **Hu B**, **Wang Y**, **Li X.** Exosomes secreted by human-induced pluripotent stem cell-derived mesenchymal stem cells repair critical-sized bone defects through

enhanced angiogenesis and osteogenesis in osteoporotic rats. *Int J Biol Sci* 12: 836–849, 2016. doi:10.7150/ijbs.14809.
26. **Gao M**, **Gao W**, **Papadimitriou JM**, **Zhang C**, **Gao J**, **Zheng M.** Exosomes—the enigmatic regulators of bone homeostasis. *Bone Res* 6: 36, 2018 [Erratum in *Bone Res* 7: 3, 2019]. doi:10.1038/s41413-018-0039-2.
27. **Fuloria S**, **Subramaniyan V**, **Dahiya R**, **Dahiya S**, **Sudhakar K**, **Kumari U**, **Sathasivam K**, **Meenakshi DU**, **Wu YS**, **Sekar M**, **Malviya R**, **Singh A**, **Fuloria NK.** Mesenchymal stem cell-derived extracellular vesicles: regenerative potential and challenges. *Biology (Basel)* 10: 172, 2021. doi:10.3390/biology10030172.
28. **Shapiro IM**, **Landis WJ**, **Risbud MV.** Matrix vesicles: are they anchored exosomes? *Bone* 79: 29–36, 2015. doi:10.1016/j.bone.2015.05.013.
29. **Ansari S**, **de Wildt BWM**, **Vis MAM**, **de Korte CE**, **Ito K**, **Hofmann S**, **Yuana Y.** Matrix vesicles: role in bone mineralization and potential use as therapeutics. *Pharmaceuticals (Basel)* 14: 289, 2021. doi:10.3390/ph14040289.
30. **Skelton AM**, **Cohen DJ**, **Boyan BD**, **Schwartz Z.** Osteoblast-derived matrix vesicles exhibit exosomal traits and a unique subset of microRNA: their caveolae-dependent endocytosis results in reduced osteogenic differentiation. *Int J Mol Sci* 24: 12770, 2023. doi:10.3390/ijms241612770.
31. **Zhang X**, **Zhao Q**, **Zhou N**, **Liu Y**, **Qin K**, **Buhl EM**, **Wang X**, **Hildebrand F**, **Balmayor ER**, **Greven J.** Osteoblast derived extracellular vesicles induced by dexamethasone: a novel biomimetic tool for enhancing osteogenesis in vitro. *Front Bioeng Biotechnol* 11: 1160703, 2023. doi:10.3389/fbioe.2023.1160703.
32. **Mebarek S**, **Buchet R**, **Pikula S**, **Strzelecka-Kiliszek A**, **Brizuela L**, **Corti G**, **Collacchi F**, **Anghieri G**, **Magrini A**, **Ciancaglini P**, **Millan JL**, **Davies O**, **Bottini M.** Do media extracellular vesicles and extracellular vesicles bound to the extracellular matrix represent distinct types of vesicles? *Biomolecules* 14: 42, 2023. doi:10.3390/biom14010042.
33. **Balcerzak M**, **Radisson J**, **Azzar G**, **Farlay D**, **Boivin G**, **Pikula S**, **Buchet R.** A comparative analysis of strategies for isolation of matrix vesicles. *Anal Biochem* 361: 176–182, 2007. doi:10.1016/j.ab.2006.10.001.
34. **Théry C**, **Amigorena S**, **Raposo G**, **Clayton A.** Isolation and characterization of exosomes from cell culture supernatants and biological fluids. *Curr Protoc Cell Biol* 30: 3.22.1–3.22.29, 2006. doi:10.1002/0471143030.cb0322s30.
35. **Jehan F**, **Zarka M**, **de la Houssaye G**, **Veziers J**, **Ostertag A**, **Cohen-Solal M**, **Geoffroy V.** New insights into the role of matrix metalloproteinase 3 (MMP3) in bone. *FASEB Bioadv* 4: 524–538, 2022. doi:10.1096/fba.2021-00092.
36. **Poullet P**, **Carpentier S**, **Barillot E.** myProMS, a web server for management and validation of mass spectrometry-based proteomic data. *Proteomics* 7: 2553–2556, 2007. doi:10.1002/pmic.200600784.
37. **The M**, **MacCoss MJ**, **Noble WS**, **Käll L.** Fast and accurate protein false discovery rates on large-scale proteomics data sets with percolator 3.0. *J Am Soc Mass Spectrom* 27: 1719–1727, 2016. doi:10.1007/s13361-016-1460-7.
38. **Valot B**, **Langella O**, **Nano E**, **Zivy M.** MassChroQ: a versatile tool for mass spectrometry quantification. *Proteomics* 11: 3572–3577, 2011. doi:10.1002/pmic.201100120.
39. **Cox J**, **Hein MY**, **Luber CA**, **Paron I**, **Nagaraj N**, **Mann M.** Accurate proteome-wide label-free quantification by delayed normalization and maximal peptide ratio extraction, termed MaxLFQ. *Mol Cell Proteomics* 13: 2513–2526, 2014. doi:10.1074/mcp.M113.031591.
40. **Josse J**, **Husson F.** missMDA: a package for handling missing values in multivariate data analysis. *J Stat Soft* 70, 2016. doi:10.18637/jss.v070.i01.
41. **Szklarczyk D**, **Franceschini A**, **Wyder S**, **Forslund K**, **Heller D**, **Huerta-Cepas J**, **Simonovic M**, **Roth A**, **Santos A**, **Tsafou KP**, **Kuhn M**, **Bork P**, **Jensen LJ**, **von Mering C.** STRING v10: protein–protein interaction networks, integrated over the tree of life. *Nucleic Acids Res* 43: D447–D452, 2015. doi:10.1093/nar/gku1003.
42. **Sherman BT**, **Hao M**, **Qiu J**, **Jiao X**, **Baseler MW**, **Lane HC**, **Imamichi T**, **Chang W.** DAVID: a web server for functional enrichment analysis and functional annotation of gene lists (2021 update). *Nucleic Acids Res* 50: W216–W221, 2022. doi:10.1093/nar/gkac194.
43. **Huang DW**, **Sherman BT**, **Lempicki RA.** Systematic and integrative analysis of large gene lists using DAVID bioinformatics resources. *Nat Protoc* 4: 44–57, 2009. doi:10.1038/nprot.2008.211.
44. **Tastsoglou S**, **Skoufos G**, **Miliotis M**, **Karagkouni D**, **Koutsoukos I**, **Karavangeli A**, **Kardaras FS**, **Hatzigeorgiou AG.** DIANA-miRPath v4.0: expanding target-based miRNA functional analysis in cell-type and tissue contexts. *Nucleic Acids Res* 51: W154–W159, 2023. doi:10.1093/nar/gkad431.
45. Abstracts of the ECTS 2024 Congress. *JBMR Plus* 8: i1–i340, 2024. doi:10.1093/jbmrpl/ziae063.
46. **Crescitelli R**, **Lässer C**, **Lötvall J.** Isolation and characterization of extracellular vesicle subpopulations from tissues. *Nat Protoc* 16: 1548–1580, 2021. doi:10.1038/s41596-020-00466-1.
47. **Wang ZX**, **Luo ZW**, **Li FXZ**, **Cao J**, **Rao SS**, **Liu YW**, **Wang YY**, **Zhu GQ**, **Gong JS**, **Zou JT**, **Wang Q**, **Tan YJ**, **Zhang Y**, **Hu Y**, **Li YY**, **Yin H**, **Wang XK**, **He ZH**, **Ren L**, **Liu ZZ**, **Hu XK**, **Yuan LQ**, **Xu R**, **Chen CY**, **Xie H.** Aged bone matrix-derived extracellular vesicles as a messenger for calcification paradox. *Nat Commun* 13: 1453, 2022. doi:10.1038/s41467-022-29191-x.
48. **Zhang C**, **Xu S**, **Zhang S**, **Liu M**, **Du H**, **Sun R**, **Jing B**, **Sun Y.** Ageing characteristics of bone indicated by transcriptomic and exosomal proteomic analysis of cortical bone cells. *J Orthop Surg Res* 14: 129, 2019. doi:10.1186/s13018-019-1163-4.
49. **Wagner KT**, **Radisic M.** A new role for extracellular vesicles in cardiac tissue engineering and regenerative medicine. *Adv Nanobiomed Res* 1: 2100047, 2021. doi:10.1002/anbr.202100047.
50. **Gupta S**, **Rawat S**, **Arora V**, **Kottarath SK**, **Dinda AK**, **Vaishnav PK**, **Nayak B**, **Mohanty S.** An improvised one-step sucrose cushion ultracentrifugation method for exosome isolation from culture supernatants of mesenchymal stem cells. *Stem Cell Res Ther* 9: 180, 2018. doi:10.1186/s13287-018-0923-0.
51. **Bazzan E**, **Tinè M**, **Casara A**, **Biondini D**, **Semenzato U**, **Cocconcelli E**, **Balestro E**, **Damin M**, **Radu CM**, **Turato G**, **Baraldo S**, **Simioni P**, **Spagnolo P**, **Saetta M**, **Cosio MG.** Critical review of the evolution of extracellular vesicles' knowledge: from 1946 to today. *Int J Mol Sci* 22: 6417, 2021. doi:10.3390/ijms22126417.
52. **Jimenez L**, **Yu H**, **McKenzie AJ**, **Franklin JL**, **Patton JG**, **Liu Q**, **Weaver AM.** Quantitative proteomic analysis of small and large extracellular vesicles (EVs) reveals enrichment of adhesion proteins in small EVs. *J Proteome Res* 18: 947–959, 2019. doi:10.1021/acs.jproteome.8b00647.
53. **Lischnig A**, **Bergqvist M**, **Ochiya T**, **Lässer C.** Quantitative proteomics identifies proteins enriched in large and small extracellular vesicles. *Mol Cell Proteomics* 21: 100273–102022, 2022 [Erratum in *Mol Cell Proteomics* 22: 100516, 2023]. doi:10.1016/j.mcpro.2022.100273.
54. **Teng F**, **Fussenegger M.** Shedding light on extracellular vesicle biogenesis and bioengineering. *Adv Sci (Weinh)* 8: 2003505, 2020. doi:10.1002/advs.202003505.
55. **Brisson AR**, **Tan S**, **Linares R**, **Gounou C**, **Arraud N.** Extracellular vesicles from activated platelets: a semiquantitative cryo-electron microscopy and immuno-gold labeling study. *Platelets* 28: 263–271, 2017. doi:10.1080/09537104.2016.1268255.
56. **Hough KP**, **Trevor JL**, **Strenkowski JG**, **Wang Y**, **Chacko BK**, **Tousif S**, **Chanda D**, **Steele C**, **Antony VB**, **Dokland T**, **Ouyang X**, **Zhang J**, **Duncan SR**, **Thannickal VJ**, **Darley-Usmar VM**, **Deshane JS.** Exosomal transfer of mitochondria from airway myeloid-derived regulatory cells to T cells. *Redox Biol* 18: 54–64, 2018. doi:10.1016/j.redox.2018.06.009.
57. **Gurung S**, **Perocheau D**, **Touramanidou L**, **Baruteau J.** The exosome journey: from biogenesis to uptake and intracellular signalling. *Cell Commun Signal* 19: 47, 2021. doi:10.1186/s12964-021-00730-1.
58. **Chen Y**, **Zhao Y**, **Yin Y**, **Jia X**, **Mao L.** Mechanism of cargo sorting into small extracellular vesicles. *Bioengineered* 12: 8186–8201, 2021. doi:10.1080/21655979.2021.1977767.
59. **Huang Y**, **Cheng L**, **Turchinovich A**, **Mahairaki V**, **Troncoso JC**, **Pletniková O**, **Haughey NJ**, **Vella LJ**, **Hill AF**, **Zheng L**, **Witwer KW.** Influence of species and processing parameters on recovery and content of brain tissue-derived extracellular vesicles. *J Extracell Vesicles* 9: 1785746, 2020. doi:10.1080/20013078.2020.1785746.
60. **Bottini M**, **Mebarek S**, **Anderson KL**, **Strzelecka-Kiliszek A**, **Bozycki L**, **Simão AMS**, **Bolean M**, **Ciancaglini P**, **Pikula JB**, **Pikula S**, **Magne D**, **Volkmann N**, **Hanein D**, **Millán JL**, **Buchet R.** Matrix vesicles from chondrocytes and osteoblasts: their biogenesis, properties, functions and biomimetic models. *Biochim Biophys Acta Gen Subj* 1862: 532–546, 2018. doi:10.1016/j.bbagen.2017.11.005.

61. **Hasegawa T.** Ultrastructure and biological function of matrix vesicles in bone mineralization. *Histochem Cell Biol* 149: 289–304, 2018. doi:10.1007/s00418-018-1646-0.
62. **Vaughan TJ**, **Verbruggen SW**, **McNamara LM.** Are all osteocytes equal? Multiscale modelling of cortical bone to characterise the mechanical stimulation of osteocytes. *Int J Numer Method Biomed Eng* 29: 1361–1372, 2013. doi:10.1002/cnm.2578.
63. **Palumbo C**, **Ferretti M.** The osteocyte: from "Prisoner" to "Orchestrator. *J Funct Morphol Kinesiol* 6: 28, 2021. doi:10.3390/jfmk6010028.
64. **Youlten SE**, **Kemp JP**, **Logan JG**, **Ghirardello EJ**, **Sergio CM**, **Dack MRG**, **et al.** Osteocyte transcriptome mapping identifies a molecular landscape controlling skeletal homeostasis and susceptibility to skeletal disease. *Nat Commun* 12: 2444, 2021. doi:10.1038/s41467-021-22517-1.
65. **Paic F**, **Igwe JC**, **Nori R**, **Kronenberg MS**, **Franceschetti T**, **Harrington P**, **Kuo L**, **Shin D-G**, **Rowe DW**, **Harris SE**, **Kalajzic I.** Identification of differentially expressed genes between osteoblasts and osteocytes. *Bone* 45: 682–692, 2009. doi:10.1016/j.bone.2009.06.010.
66. **Wang JS**, **Wein MN.** Pathways controlling formation and maintenance of the osteocyte dendrite network. *Curr Osteoporos Rep* 20: 493–504, 2022. doi:10.1007/s11914-022-00753-8.
67. **Delorme G**, **Saltel F**, **Bonnelye E**, **Jurdic P**, **Machuca-Gayet I.** Expression and function of semaphorin 7A in bone cells. *Biol Cell* 97: 589–597, 2005. doi:10.1042/BC20040103.
68. **Zhang Y**, **Shen S**, **Li P**, **Fan Y**, **Zhang L**, **Li W**, **Liu Y.** PLEXIN-B2 promotes the osteogenic differentiation of human bone marrow mesenchymal stem cells via activation of the RhoA signaling pathway. *Cell Signal* 62: 109343, 2019. doi:10.1016/j.cellsig.2019.06.008.
69. **Plotkin LI**, **Wallace JM.** MicroRNAs and osteocytes. *Bone* 150: 115994, 2021. doi:10.1016/j.bone.2021.115994.
70. **Zeng Q**, **Wang Y**, **Gao J**, **Yan Z**, **Li Z**, **Zou X**, **Li Y**, **Wang J**, **Guo Y.** miR-29b-3p regulated osteoblast differentiation via regulating IGF-1 secretion of mechanically stimulated osteocytes. *Cell Mol Biol Lett* 24: 11, 2019. doi:10.1186/s11658-019-0136-2.
71. **Uenaka M**, **Yamashita E**, **Kikuta J**, **Morimoto A**, **Ao T**, **Mizuno H**, **Furuya M**, **Hasegawa T**, **Tsukazaki H**, **Sudo T**, **Nishikawa K**, **Okuzaki D**, **Motooka D**, **Kosaka N**, **Sugihara F**, **Boettger T**, **Braun T**, **Ochiya T**, **Ishii M.** Osteoblast-derived vesicles induce a switch from bone-formation to bone-resorption in vivo. *Nat Commun* 13: 1066, 2022. doi:10.1038/s41467-022-28673-2.
72. **Morhayim J**, **van de Peppel J**, **Braakman E**, **Rombouts EWJC**, **ter Borg MND**, **Dudakovic A**, **Chiba H**, **van der Eerden BCJ**, **Raaijmakers MH**, **van Wijnen AJ**, **Cornelissen JJ**, **van Leeuwen JP.** Osteoblasts secrete miRNA-containing extracellular vesicles that enhance expansion of human umbilical cord blood cells. *Sci Rep* 6: 32034, 2016. doi:10.1038/srep32034.
73. **Huang K**, **Fu J**, **Zhou W**, **Li W**, **Dong S**, **Yu S**, **Hu Z**, **Wang H**, **Xie Z.** MicroRNA-125b regulates osteogenic differentiation of mesenchymal stem cells by targeting Cbfβ in vitro. *Biochimie* 102: 47–55, 2014. doi:10.1016/j.biochi.2014.02.005.
74. **Wang H**, **Xie Z**, **Hou T**, **Li Z**, **Huang K**, **Gong J**, **Zhou W**, **Tang K**, **Xu J**, **Dong S.** MiR-125b regulates the osteogenic differentiation of human mesenchymal stem cells by targeting BMPR1b. *Cell Physiol Biochem* 41: 530–542, 2017. doi:10.1159/000457013.
75. **Weivoda MM**, **Lee S-K**, **Monroe DG.** miRNAs in osteoclast biology. *Bone* 143: 115757, 2021. doi:10.1016/j.bone.2020.115757.
76. **Materozzi M**, **Resnati M**, **Facchi C**, **Trudu M**, **Orfanelli U**, **Perini T**, **Gennari L**, **Milan E**, **Cenci S.** A novel proteomic signature of osteoclast differentiation unveils the deubiquitinase UCHL1 as a necessary osteoclastogenic driver. *Sci Rep* 14: 7290, 2024. doi:10.1038/s41598-024-57898-y.
77. **Zhao C**, **Sun W**, **Zhang P**, **Ling S**, **Li Y**, **Zhao D**, **Peng J**, **Wang A**, **Li Q**, **Song J**, **Wang C**, **Xu X**, **Xu Z**, **Zhong G**, **Han B**, **Chang Y-Z**, **Li Y.** miR-214 promotes osteoclastogenesis by targeting Pten/PI3k/Akt pathway. *RNA Biol* 12: 343–353, 2015. doi:10.1080/15476286.2015.1017205.
78. **Schneider P**, **Krucker T**, **Meyer E**, **Ulmann-Schuler A**, **Weber B**, **Stampanoni M**, **Müller R.** Simultaneous 3D visualization and quantification of murine bone and bone vasculature using micro-computed tomography and vascular replica. *Microsc Res Tech* 72: 690–701, 2009. doi:10.1002/jemt.20720.
79. **Zhivodernikov IV**, **Markina YV**, **Kirichenko TV**, **Popov MA**, **Markin AM.** Exosomes as a potential therapeutic approach in osteoimmunology. *Front Immunol* 14: 1309015, 2023. doi:10.3389/fimmu.2023.1309015.
80. **Mathieu M**, **Martin-Jaular L**, **Lavieu G**, **Théry C.** Specificities of secretion and uptake of exosomes and other extracellular vesicles for cell-to-cell communication. *Nat Cell Biol* 21: 9–17, 2019. doi:10.1038/s41556-018-0250-9.
81. **Lamprou M**, **Kaspiris A**, **Panagiotopoulos E**, **Giannoudis PV**, **Papadimitriou E.** The role of pleiotrophin in bone repair. *Injury* 45: 1816–1823, 2014. doi:10.1016/j.injury.2014.10.013.
82. **Günther T**, **Poli C**, **Müller JM**, **Catala-Lehnen P**, **Schinke T**, **Yin N**, **Vomstein S**, **Amling M**, **Schüle R.** Fhl2 deficiency results in osteopenia due to decreased activity of osteoblasts. *EMBO J* 24: 3049–3056, 2005. doi:10.1038/sj.emboj.7600773.
83. **Brun J**, **Dieudonné F-X**, **Marty C**, **Müller J**, **Schüle R**, **Patiño-García A**, **Lecanda F**, **Fromigué O**, **Marie PJ.** FHL2 silencing reduces Wnt signaling and osteosarcoma tumorigenesis in vitro and in vivo. *PLoS One* 8: e55034, 2013. doi:10.1371/journal.pone.0055034.
84. **Foster LJ**, **Zeemann PA**, **Li C**, **Mann M**, **Jensen ON**, **Kassem M.** Differential expression profiling of membrane proteins by quantitative proteomics in a human mesenchymal stem cell line undergoing osteoblast differentiation. *Stem Cells* 23: 1367–1377, 2005. doi:10.1634/stemcells.2004-0372.
85. **Vimalraj S**, **Partridge NC**, **Selvamurugan N.** A positive role of microRNA-15b on regulation of osteoblast differentiation. *J Cell Physiol* 229: 1236–1244, 2014. doi:10.1002/jcp.24557.
86. **Zhang F**, **Cao K**, **Du G**, **Zhang Q**, **Yin Z.** miR-29a promotes osteoblast proliferation by downregulating DKK-1 expression and activating Wnt/β-catenin signaling pathway. *Adv Clin Exp Med* 28: 1293–1300, 2019. doi:10.17219/acem/104533.
87. **Lin Y-P**, **Liao L-M**, **Liu Q-H**, **Ni Y**, **Zhong Y**, **Yu S.** MiRNA-128-3p induces osteogenic differentiation of bone marrow mesenchymal stem cells via activating the Wnt3a signaling. *Eur Rev Med Pharmacol Sci* 25: 1225–1232, 2021. doi:10.26355/eurrev_202102_24826.
88. **Roberto VP**, **Tiago DM**, **Silva IAL**, **Cancela ML.** MiR-29a is an enhancer of mineral deposition in bone-derived systems. *Arch Biochem Biophys* 564: 173–183, 2014. doi:10.1016/j.abb.2014.09.006.
89. **Kulterer B**, **Friedl G**, **Jandrositz A**, **Sanchez-Cabo F**, **Prokesch A**, **Paar C**, **Scheideler M**, **Windhager R**, **Preisegger KH**, **Trajanoski Z.** Gene expression profiling of human mesenchymal stem cells derived from bone marrow during expansion and osteoblast differentiation. *BMC Genomics* 8, 2007. doi:10.1186/1471-2164-8-70.
90. **Go W**, **Korzh V.** Plasma membrane Ca^{2+} ATPase Atp2b1a regulates bone mineralization in zebrafish. *Bone* 54: 48–57, 2013. doi:10.1016/j.bone.2013.01.026.
91. **Wang W**, **Li F**, **Wang K**, **Cheng B**, **Guo X.** PAPSS2 promotes alkaline phosphates activity and mineralization of osteoblastic MC3T3-E1 cells by crosstalk and Smads signal pathways. *PLoS One* 7: e43475, 2012. doi:10.1371/journal.pone.0043475.
92. **Ren S**, **Lin Y**, **Liu W**, **Yang L**, **Zhao M.** MSC-Exos: important active factor of bone regeneration. *Front Bioeng Biotechnol* 11: 1136453, 2023. doi:10.3389/fbioe.2023.1136453.
93. **Man K**, **Eisenstein NM**, **Hoey DA**, **Cox SC.** Bioengineering extracellular vesicles: smart nanomaterials for bone regeneration. *J Nanobiotechnology* 21: 137, 2023. doi:10.1186/s12951-023-01895-2.
94. **Perez-Riverol Y**, **Bai J**, **Bandla C**, **García-Seisdedos D**, **Hewapathirana S**, **Kamatchinathan S**, **Kundu DJ**, **Prakash A**, **Frericks-Zipper A**, **Eisenacher M**, **Walzer M**, **Wang S**, **Brazma A**, **Vizcaíno JA.** The PRIDE database resources in 2022: a hub for mass spectrometry-based proteomics evidences. *Nucleic Acids Res* 50: D543–D552, 2022. doi:10.1093/nar/gkab1038.